INTERNATIONAL JOURNAL FOR NUMERICAL AND ANALYTICAL METHODS IN GEOMECHANICS
Int. J. Numer. Anal. Meth. Geomech. 2000; **00**:1–6 *Prepared using* nagauth.cls *[Version: 2002/09/18 v1.02]*

Computational Model Coupling Mode II Discrete Fracture Propagation with Continuum Damage Zone Evolution

Wencheng Jin[1], Hao Xu[2], Chloé Arson[1,*], Seth Busetti[3]

[1] *School of Civil and Environmental Engineering, Georgia Institute of Technology, GA, USA*
[2] *Lawrence Berkeley National Laboratory, CA, USA*
[3] *ConocoPhillips, Houston, TX, USA*

SUMMARY

We propose a numerical method that couples a Cohesive Zone Model (CZM) and a Finite Element - based Continuum Damage Mechanics (CDM) model. The CZM represents a mode II macro-fracture, and CDM Finite Elements (FE) represent the damage zone of the CZM. The coupled CZM/CDM model can capture the flow of energy that takes place between the bulk material that forms the matrix and the macroscopic fracture surfaces. The CDM model, which does not account for micro-crack interaction, is calibrated against triaxial compression tests performed on Bakken shale, so as to reproduce the stress/strain curve before the failure peak. Based on a comparison with Kachanov's micro-mechanical model, we confirm that the critical microcrack density value equal to 0.3 reflects the point at which crack interaction cannot be neglected. The CZM is assigned a pure mode II cohesive law which accounts for the dependence of the shear strength and energy release rate on confining pressure. The cohesive shear strength of the CZM is calibrated by calculating the shear stress necessary to reach a CDM damage of 0.3 during a direct shear test. We find that the shear cohesive strength of the CZM depends linearly on the confining pressure. Triaxial compression tests are simulated, in which the shale sample is modeled as a FE CDM continuum that contains a predefined thin cohesive zone representing the idealized shear fracture plane. The shear energy release rate of the CZM is fitted in order to match to the post-peak stress/strain curves obtained during experimental tests performed on Bakken shale. We find that the energy release rate depends linearly on the shear cohesive strength. We then use the calibrated shale rheology to simulate the propagation of a meter-scale mode II fracture. Under low confining pressure, the macroscopic crack (CZM) and its damaged zone (CDM) propagate simultaneously (i.e. during the same loading increments). Under high confining pressure, the fracture propagates in slip-friction, i. e. the debonding of the cohesive zone alternates with the propagation of continuum damage. The computational method is applicable to a range of geological injection problems including hydraulic fracturing and fluid storage, and should be further enhanced by the addition of mode I and mixed mode (I+II+III) propagation.

KEY WORDS: Fracture Mechanics; Continuum Damage Mechanics; Finite Element Method, Cohesive Zone Model; Energy dissipation; Upscaling

*Correspondence to: Chloé Arson
Email: chloe.arson@ce.gatech.edu

Contract/grant sponsor:

Received
Revised
Accepted

1. INTRODUCTION

In numerical methods, cavities, faults and fractures are usually modeled as separated or weakly bonded surfaces [1, 2], or as notch-shaped flaws [3]. The corresponding governing equations are primarily based on Fracture Mechanics (FM). For instance, fractures are usually represented by Griffith macroscopic cracks, which open or slide under the influence of a differential stress [4]. In classical FM, the fracture is assumed to propagate when the Stress Intensity Factor (SIF) (respectively the strain energy release rate) reaches the fracture toughness (respectively the strength of the bounding material) at the crack tip [5]. Such propagation criteria are only valid for purely elastic materials. In non-elastic continua, models require that the maximum size of the plastic or damage zone near the fracture tip be smaller than the specimen or domain dimensions by at least two orders of magnitude. In Continuum Damage Mechanics (CDM), models were either based on phenomenology [6, 7] or grounded on micromechanics [8, 9]. At the scale of the Representative Elementary Volume (REV), CDM models were proposed to account for unilateral effects [10, 11], microcrack friction [12] and strength difference in tension and compression [13]. CDM models were also formulated with sophisticated damage internal variables (e.g. anisotropic damage tensors [14] and discrete sets of damage tensors [15]) in order to represent the evolution of the process zone, i.e. the area surrounding the crack tip that undergoes inelastic deformation. For materials that undergo significant inelastic deformation, the Crack Tip Open Displacement (CTOD) method, the J-integral method [16] and Cohesive Zone Models (CZM) [17, 18] are more suitable to model macroscale fracture propagation.

The concept of cohesive zone was introduced by Barenblatt [19], and was used since then to study different types of failure mechanisms. Xu and Needleman [20] used exponential shaped traction-separation models to study the fast growth of cracks in brittle materials under dynamic loading. Hutchinson et al [21, 22, 23] used a trapezoidal shaped traction-separation model to calculate the crack growth resistance in elasto-plastic materials. The bilinear cohesive zone model was used to predict the behavior of brittle materials, for example to simulate hydraulic fracturing in rocks [2] and to explain fracture patterns in concrete [24]. Paulino et al. formulated unified potential-based CZMs to study asphalt and concrete [25, 26, 27, 28]. CZMs are widely used and computationally efficient. In CZMs, the damage path is predefined [29, 30] and the presence of smaller-scale discontinuities in the damage process zone is not accounted for [31]. While the need for an *a priori* definition of the crack location limits the problems to predictable and idealized propagation paths, using the CZM method allows testing and refining the coupling algorithms between the micro and macroscales without the added numerical complexity intrinsic to other discrete fracture methods (e.g., XFEM, discrete elements, particle codes, etc.). Namely, our present focus is to better simulate the propagation of a discrete geometric fracture within a damaged region of rock.

Indeed, neglecting the effects of micro-cracks leads to ignoring the stiffness degradation of the bounding material, and therefore, to under-estimating fracture propagation. A representation of rock microstructure, at the scale of the material internal length, is needed to relate the extent of the damaged zone to the density, size and shape of the cracks. Recent studies established an explicit relationship between rock grain size distribution and the dimensions of the fracture process zone [32]. Multiscale strategies were also proposed to couple fracture mechanics criteria with a CDM model to represent the evolution of micro-cracks in the bounding material. For instance, Valkó and Economides [33, 34] calculated the velocity of the tip of a hydraulic

fracture by using a SIF that depends on a scalar damage variable. Mazars and Pijaudier-Cabot [35] established an equivalence between the energy dissipated by opening a discrete fracture and the energy dissipated by a dilute distribution of micro-cracks. Based on similar thermodynamic principles, Jiràsek and Zimmermann [36, 37] used a non-local damage model to predict micro-crack propagation and the transition to cohesive zone debonding due to micro-crack coalescence. Comi et al. [38, 39] used the value and the gradient of nonlocal damage in order to predict the transition between smeared continuum damage propagation and discrete fracture growth, and to calculate the propagation direction of the macro-fracture. The energy dissipated by CZM debonding is equivalent to that dissipated by CDM non-local damage propagation in the absence of coalescence. An Extended FE method was presented in [40], in which local damage is predicted by a gradient-enhanced CDM model. When local damage reaches unity (usually around the fracture tip), the Finite Element is split along the direction of maximum non-local equivalent strain. Cazes et al. [41] found a method to derive the shape of the debonded cohesive zone from non-local damage. Cuvilliez et al. [42] designed a flexible modeling framework, in which the transition between continuum damage and discrete fracture can be set for any REV size. The computational method explained in [43] relies on homogenization: macro-fracture propagation is upscaled from the micro-crack density tensor. Note that in all the multiscale modeling strategies listed, an internal length parameter is explicitly introduced in the formulation, which prevents damage localization and mesh dependency problems when simulating the softening response.

In the following study, we propose a numerical method that couples a CDM model (for the bulk) to a Cohesive Zone Model (for the fracture), in order to simulate the propagation of a discrete mode II fracture within a damaged zone. In Section 2, we provide an analysis of the dissipation processes that are represented during crack propagation in the CZM and in the CDM Differential Stress Induced Damage (DSID) model [7, 44]. Then we calibrate the CZM/CDM model so as to reproduce the stress/strain curves of Bakken shale during typical triaxial compression tests. Bakken shale is a tight organic reservoir rock that exhibits representative deformation curves common to many rocks that undergo hydraulic fracturing. We present the calibration method for the behavior simulated before the failure peak (Section 3) and after the failure peak (Section 4). In Section 5, we calculate the propagation rate of a mode II fracture embedded in a meter-scale damaged zone.

2. THEORETICAL FRAMEWORK OF THE COUPLED MODEL OF DAMAGE AND FRACTURE PROPAGATION

2.1. Continuum Damage Mechanics model

In most continuum mechanics models of anisotropic damage, the free energy postulated for the solid skeleton is expressed in terms of deformation. As a result, the damage work-conjugate variable $\mathbf{Y}$ (called energy release rate or damage driving force in the following) is also a function of deformation [45, 46, 47, 48]. In order to better account for states of tensile deformation under differential stress, we use the DSID model (Differential Stress Induced Damage model), in which the free energy potential is expressed as a function of stress [7]. The damage tensor (noted $\boldsymbol{\Omega}$) is a phenomenological internal variable, which controls the degradation of material stiffness along principal crack planes. The Gibbs free energy (G_s) is the sum of the damaged

elastic deformation energy stored in the material, the potential energy that can be released by creating new material surfaces, and the potential energy that can be released by opening cracks (i.e., potential irreversible deformation energy). This free energy potential is expressed as a polynomial that is quadratic in stress and linear in damage, which implies that the material is linear elastic in the absence of damage [49, 6]. The thermodynamic framework of the DSID model is summarized in Table I. Stress/strain relationships are obtained by deriving the Gibbs free energy by stress. Damage evolution is controlled by a damage function, similar to the Drucker-Prager yield function (expressed in terms of energy release rate instead of stress). The damage flow rule is non-associate, and the damage potential is chosen so as to ensure the positivity of dissipation associated to damage. The irreversible deformation due to damage follows an associated flow rule, which ensures that dilation due to crack opening takes place in the damage principal directions (i.e. in the directions orthogonal to the crack planes). With sustained deformation, it is anticipated that a non-associative flow rule would be needed to capture shear dilatancy. We captured the resulting shear localization by coupling the DSID model to a CZM of discrete fracture. Irreversible shear strains calculated with the DSID model were considered small enough to justify the use of the DSID associate flow rule.

At the scale of a continuum REV (i.e. at the material point), the energy dissipated by damage can be calculated from the Inequality of Clausius-Duhem:

$$\begin{aligned} \dot{\Phi}_s &= \boldsymbol{\sigma} : \dot{\boldsymbol{\varepsilon}} - \dot{\psi}_s = \boldsymbol{\sigma} : \dot{\boldsymbol{\varepsilon}}^{id} + \boldsymbol{Y} : \dot{\boldsymbol{\Omega}} \geq 0. \\ \int \dot{\Phi}_s \, \mathrm{d}t &= \int \boldsymbol{\sigma} : \dot{\boldsymbol{\varepsilon}} \, \mathrm{d}t - \frac{1}{2}\boldsymbol{\sigma} : \boldsymbol{\varepsilon}^E = \int \boldsymbol{\sigma} : \dot{\boldsymbol{\varepsilon}}^{id} \, \mathrm{d}t + \int \boldsymbol{Y} : \dot{\boldsymbol{\Omega}} \, \mathrm{d}t \geq 0 \end{aligned} \tag{1}$$

Where ψ_s is Helmholtz free energy (defined as the Legendre transform of Gibbs energy), and $\boldsymbol{\sigma} : \dot{\boldsymbol{\varepsilon}}$ is the incremental deformation power (equal to the power provided by external forces to the REV). The total dissipated energy $\int \dot{\Phi}_s \, \mathrm{d}t$ is the difference between external work and recoverable strain energy, $\frac{1}{2}\boldsymbol{\sigma} : \boldsymbol{\varepsilon}^E$. Note that in the DSID model, the total elastic deformation $\boldsymbol{\varepsilon}^E$ is the sum of the purely elastic deformation $\boldsymbol{\varepsilon}^{el}$ (deformation undergone by the material in the absence of damage) and of the damaged elastic deformation $\boldsymbol{\varepsilon}^{ed}$ (additional recoverable deformation caused by material softening). As shown in Figure 1, the decomposition of deformation allows accounting for two types of energy dissipation processes: micro-crack debonding causing stiffness degradation but no irreversible deformation (term $\int \boldsymbol{Y} : \dot{\boldsymbol{\Omega}} \, \mathrm{d}t$); and micro-crack opening resulting in residual irreversible strains (term $\int \boldsymbol{\sigma} : \dot{\boldsymbol{\varepsilon}}^{id} \, \mathrm{d}t$).

2.2. Cohesive Zone Model

The DSID model assumes that micro-cracks do not interact; this assumption does not hold when damage exceeds a critical value $\boldsymbol{\Omega}_{cr}$. In order to overcome this limitation, we propose to couple the DSID model with a fracture mechanics model. Above the critical value $\boldsymbol{\Omega}_{cr}$, continuum damage is replaced by a cohesive law (CZM) assigned to a local area representing an initially bonded discrete crack with properties set equivalent to the damaged bulk material at the damage threshold $\boldsymbol{\Omega}_{cr}$. As the fracture faces debond according to a traction-separation law, the bulk material surrounding the discrete crack unloads, which results in partial recovery of elastic energy.

CZMs that are governed by different force-displacement curves but that have equal cohesive strength and equal cohesive energy release rate provide similar predictions of stress and strain

Table I. Thermodynamic framework of the DSID model

D.S.I.D. Model	
Free Energy	$G_s(\boldsymbol{\sigma},\boldsymbol{\Omega}) = \frac{1}{2}\boldsymbol{\sigma} : \mathbb{S}_0 : \boldsymbol{\sigma} + a_1\,\mathrm{Tr}\boldsymbol{\Omega}(\mathrm{Tr}\boldsymbol{\sigma})^2 + a_2\,\mathrm{Tr}(\boldsymbol{\sigma}\cdot\boldsymbol{\sigma}\cdot\boldsymbol{\Omega}) + a_3\,\mathrm{Tr}\boldsymbol{\sigma}\,\mathrm{Tr}(\boldsymbol{\Omega}\cdot\boldsymbol{\sigma}) + a_4\,\mathrm{Tr}\boldsymbol{\Omega}\,\mathrm{Tr}(\boldsymbol{\sigma}\cdot\boldsymbol{\sigma})$ $\boldsymbol{\varepsilon}^E = \frac{\partial G_s}{\partial \boldsymbol{\sigma}} = \frac{1+\nu_0}{E_0}\boldsymbol{\sigma} - \frac{\nu_0}{E_0}(\mathrm{Tr}\boldsymbol{\sigma})\,\boldsymbol{\delta} + 2a_1(\mathrm{Tr}\boldsymbol{\Omega}\,\mathrm{Tr}\boldsymbol{\sigma})\,\boldsymbol{\delta} + a_2(\boldsymbol{\sigma}\cdot\boldsymbol{\Omega}+\boldsymbol{\Omega}\cdot\boldsymbol{\sigma}) + a_3[\,\mathrm{Tr}(\boldsymbol{\sigma}\cdot\boldsymbol{\Omega})\,\boldsymbol{\delta} + (\mathrm{Tr}\boldsymbol{\sigma})\,\boldsymbol{\Omega}\,] + 2a_4(\mathrm{Tr}\boldsymbol{\Omega})\,\boldsymbol{\sigma}$ $\boldsymbol{Y} = \frac{\partial G_s}{\partial \boldsymbol{\Omega}} = a_1(\mathrm{Tr}\boldsymbol{\sigma})^2\,\boldsymbol{\delta} + a_2\boldsymbol{\sigma}\cdot\boldsymbol{\sigma} + a_3\mathrm{Tr}(\boldsymbol{\sigma})\boldsymbol{\sigma} + a_4\mathrm{Tr}(\boldsymbol{\sigma}\cdot\boldsymbol{\sigma})\boldsymbol{\delta}$
Damage Function	$f_d = \sqrt{J^*} - \alpha I^* - k$ $J^* = \frac{1}{2}(\mathbb{P}_1 : \boldsymbol{Y} - \frac{1}{3}I^*\boldsymbol{\delta}) : (\mathbb{P}_1 : \boldsymbol{Y} - \frac{1}{3}I^*\boldsymbol{\delta}), \quad I^* = (\mathbb{P}_1 : \boldsymbol{Y}) : \boldsymbol{\delta}$ $\mathbb{P}_1(\boldsymbol{\sigma}) = \sum_{p=1}^{3}\left[H(\sigma^{(p)}) - H(-\sigma^{(p)})\right]\boldsymbol{n}^{(p)}\otimes\boldsymbol{n}^{(p)}\otimes\boldsymbol{n}^{(p)}\otimes\boldsymbol{n}^{(p)}$ $k = C_0 - C_1\mathrm{Tr}(\boldsymbol{\Omega})$
Damage Potential	$g_d = \sqrt{\frac{1}{2}(\mathbb{P}_2 : \boldsymbol{Y}) : (\mathbb{P}_2 : \boldsymbol{Y})}$ $\mathbb{P}_2 = \sum_{p=1}^{3} H\left[\max_{q=1}^{3}(\sigma^{(q)}) - \sigma^{(p)}\right]\boldsymbol{n}^{(p)}\otimes\boldsymbol{n}^{(p)}\otimes\boldsymbol{n}^{(p)}\otimes\boldsymbol{n}^{(p)}$
Flow Rule	$\dot{\boldsymbol{\varepsilon}}^{id} = \dot{\lambda}_d\frac{\partial f_d}{\partial \boldsymbol{\sigma}} = \dot{\lambda}_d\frac{\partial f_d}{\partial \boldsymbol{Y}} : \frac{\partial \boldsymbol{Y}}{\partial \boldsymbol{\sigma}}$ $\dot{\boldsymbol{\Omega}} = \dot{\lambda}_d\frac{\partial g_d}{\partial \boldsymbol{Y}}$

G_s: Gibbs free energy	$\boldsymbol{\varepsilon}^E$: Total elastic strain	C_0: Initial damage threshold
$\boldsymbol{\sigma}$: Stress tensor	$\boldsymbol{\delta}$: Kronecker delta	$\mathbb{S}_0$: Undamaged compliance tensor
$\boldsymbol{\Omega}$: Damage variable	$\boldsymbol{Y}$: Damage driving force	$\max(\cdot)$: Maximum function
E_0: Young's Modulus	$\dot{\boldsymbol{\Omega}}$: Damage rate	C_1: Damage hardening variable
ν_0: Poisson's ratio	$H(\cdot)$: Heaviside function	a_1, a_2, a_3, a_4: Material parameters
f_d: Damage function	$\dot{\lambda}_d$: Lagrangian Multiplier	$\mathbb{P}_1$ and $\mathbb{P}_2$: Projection tensors
g_d: Damage potential	$\dot{\boldsymbol{\varepsilon}}^{id}$: Irreversible strain rate	$\sigma^{(p)}$; $\boldsymbol{n}^{(p)}$: Principal stress tensor; vector

except close to boundaries [50, 51]. The type of traction-separation law in the CZM mostly influences the stress and strain fields at the fracture tip [52]. We considered a range of real deformation tests on our test material (Bakken shale from subsurface core) and found the actual form of the traction-separation response to be difficult to constrain without more robust laboratory testing. Thus, for simplicity, we chose a bilinear CZM (Figure 2). When the cohesive strength is reached (σ_{max} in mode I, τ_{max} in mode II), the relative displacement of the fracture faces reaches the threshold value δ_0 (cohesive crack tip) and the faces of the cohesive zone start to separate. Failure (i.e. complete face separation) is reached at the material crack tip (for a relative displacement δ_f), where cohesive strength acting across the cohesive zone surfaces are equal to zero. The mechanical work needed to create a unit area of fully debonded crack is referred to as the cohesive fracture energy (noted G_c). For a sharp crack embedded in a

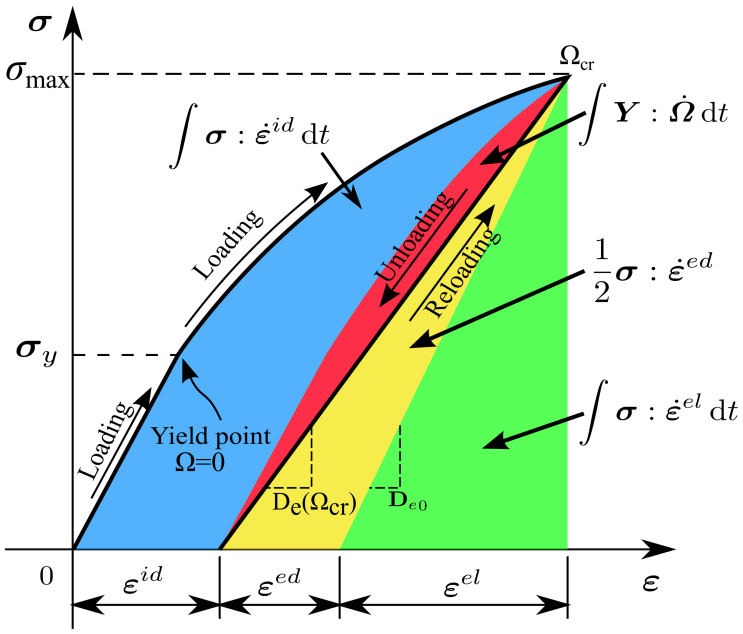

Figure 1. Evolution of energy potentials in a REV governed by the DSID model

homogeneous elastic body, G_c can be calculated as [18]:

$$G_c = \int_0^{\delta_f} \boldsymbol{\sigma} d\boldsymbol{\delta} \tag{2}$$

In elastic materials, the value of the energy release rate G_c is an intrinsic material property that can be expressed as:

$$G_c = \frac{K_{IC}^2}{E'} + \frac{K_{IIC}^2}{E'} + \frac{K_{IIIC}^2}{2G} \tag{3}$$

Where K_{IC} (respectively K_{IIC}, K_{IIIC}) is mode I (respectively mode II, mode III) fracture toughness in linear elastic fracture mechanics. $E' = E$ in plane stress and $E' = E/(1-\nu^2)$ in plane strain. Note that for most rock materials, the cohesive strength and the energy release rate depend on the confinement stress and thus need to be calibrated for various confinement pressures. Confinement also tends to reduce the the stress drop depicted in Figure 2 after the peak stress, which results in a residual shear strength. In this case the zero in the lower bound of the integral in equation 2 can be replaced with the residual shear displacement, and G_c is accordingly modified. For example, in seismicity and other dynamic studies it may be important to capture the magnitude of the shear stress-drop.

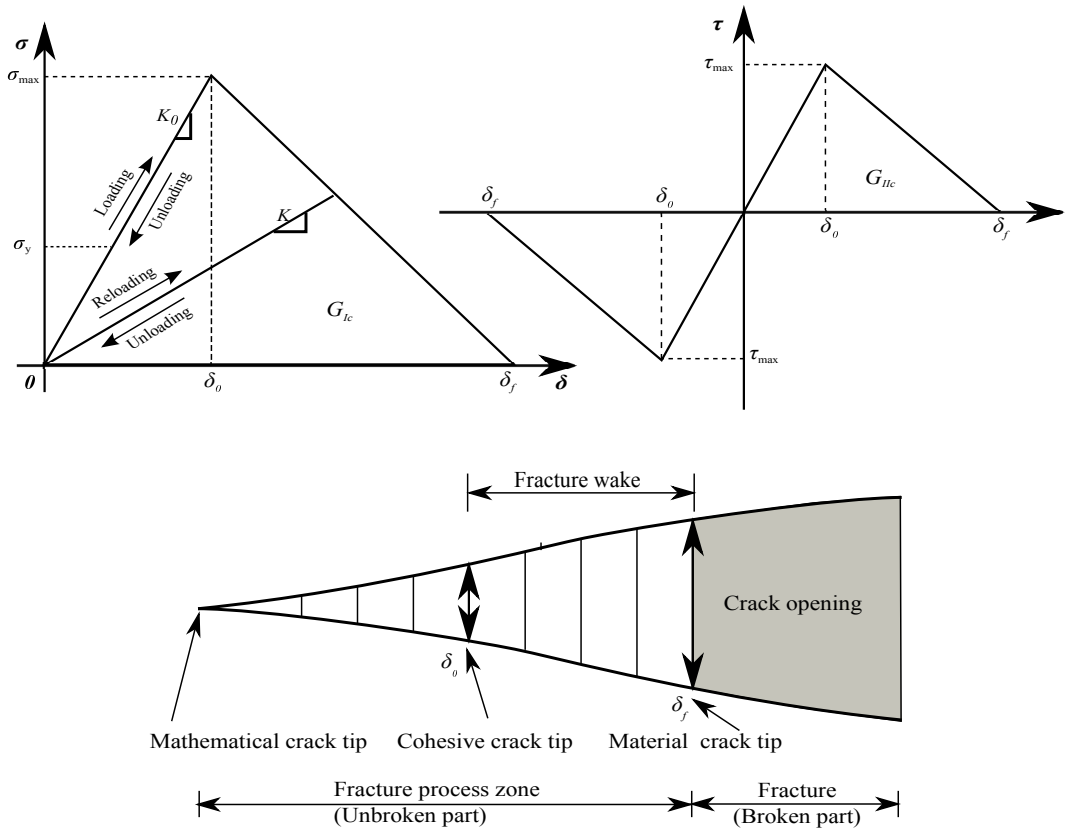

Figure 2. Bilinear Cohesive Zone Model

2.3. Transfers of energy between fracture surfaces and the damage zone

As explained in Equation 2, the energy release rate G_c is entirely dissipated in the cohesive zone if the bounding material is purely elastic. By contrast, in a material that is subject to micro-cracking, fracture propagation is both due to the micro crack initiation and debonding within the bounding material (this is accounted for with the DSID model) and to the separation of macro crack faces (this is accounted for with the CZM). In other words, the energy release rate measured during laboratory experiments includes the energy dissipated to form micro-cracks in the matrix, to produce irreversible strains in the matrix, and to propagate the macro-fracture. When a cohesive crack propagates in a damaged elastic REV, the energy balance is expressed as:

$$\begin{aligned} E_w =& E_e + E_{in} + E_c \\ =& \int_0^t \Big(\int_V \boldsymbol{\sigma} : \dot{\boldsymbol{\varepsilon}}^{el} \, \mathrm{d}V + \int_V \boldsymbol{\sigma} : \dot{\boldsymbol{\varepsilon}}^{ed} \, \mathrm{d}V \Big) \, \mathrm{d}\tau \\ &+ \int_0^t \Big(\int_V \boldsymbol{Y} : \dot{\boldsymbol{\Omega}} \, \mathrm{d}V + \int_V \boldsymbol{\sigma} : \dot{\boldsymbol{\varepsilon}}^{id} \, \mathrm{d}V \Big) \, \mathrm{d}\tau + \int_0^t \Big(\int_S \boldsymbol{\sigma} : \boldsymbol{\delta} \, \mathrm{d}S \Big) \, \mathrm{d}\tau \end{aligned} \tag{4}$$

In which E_w is the energy supplied by external work, E_c is the energy dissipated by crack debonding in the CZM, and E_e and E_{in} are respectively the stored elastic energy and the dissipated energy in the bounding material (around the cohesive crack). E_e is the sum of purely elastic deformation energy (stored in the undamaged part of the matrix) and deformation energy due to recoverable micro-crack displacement jumps at micro-crack faces. E_{in} accounts for both the debonding of micro-cracks (i.e. the creation of material surfaces in micro-cracks) and for the irreversible deformation induced by residual crack openings. We have $G_c = E_{in}+E_c$. The question is: What is the proportion of mechanical work that dissipates in the form of micro-cracks (E_{in}), and what is the proportion of mechanical work that dissipates in the form of a discrete portion of fracture (E_c)? Chandra et al. [53, 51] investigated the influence of the ratio of cohesive strength over yield strength $\boldsymbol{\sigma}_{max}/\boldsymbol{\sigma}_y$ for elastic-plastic materials. As shown in Figure 3, the plastic work takes a more important percentage of strain energy as the ratio of $\boldsymbol{\sigma}_{max}/\boldsymbol{\sigma}_y$ increases. This is commonly referred to as the brittle-ductile transition, and is evidenced in stress/strain behavior as an increasingly developed strain hardening zone and lack of a post-failure stress drop with increased confinement.

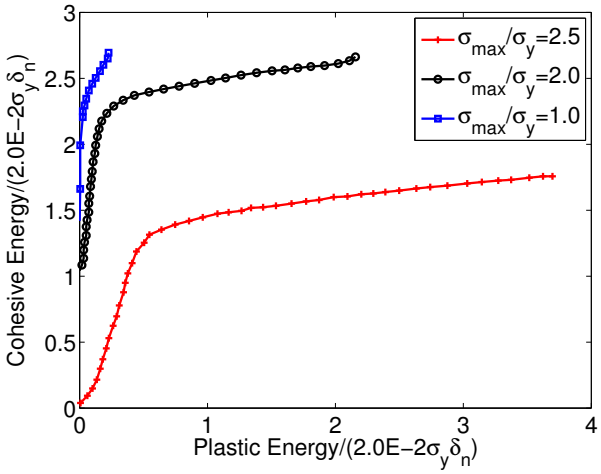

Figure 3. Evolution of the plastic energy and of the cohesive energy dissipated during crack propagation in an elasto-plastic material, with the ratio cohesive strength by yield strength $\boldsymbol{\sigma}_{max}/\boldsymbol{\sigma}_y$. Note: δ_n is the relative displacement of two faces when the traction reaches σ_y (constant) - adapted from [53].

By tracking the energy components in different patches within the bounding material and within different segments of a cohesive fracture, Shet and Chandra [53] modeled the evolution of the elastic energy E_e, the plastic energy E_p (equivalent to E_{in} in the DSID model) and the cohesive energy E_c evolution during fracture propagation. The dissipation of plastic energy (E_p) initiates when the yield stress $\boldsymbol{\sigma}_y$ is reached. When the stress in the cohesive segments reaches the cohesive strength $\boldsymbol{\sigma}_{max}$, the cohesive elements and the bounding material elements behind the tip are unloaded, plastic dissipation stops (i.e. the cumulated plastic work remains stationary), and elastic energy is recovered in the bounding material. However, the cohesive energy continues to increase until crack faces are completely debonded. The final crack length depends on the cohesive strength $\boldsymbol{\sigma}_{max}$ [51]. In the following, we calibrate the DSID model

Table II. Calibrated DSID parameters

Elasticity		Free Energy				Damage function		
E_0	ν_0	a_1	a_2	a_3	a_4	C_0	C_1	α
GPa	–	MPa^{-1}	MPa^{-1}	MPa^{-1}	MPa^{-1}	MPa	MPa	–
46	0.186	7.35×10^{-7}	1.21×10^{-4}	-3.15×10^{-11}	2.39×10^{-12}	0.01	1.18	0.399

coupled with the CZM in order to capture micro-crack propagation followed by macroscopic failure (fracture propagation) in shale. We start by determining the initial damage yield threshold (similar to $\boldsymbol{\sigma}_y$) and then, we calibrate the ultimate cohesive strength of the damaged material (similar to $\boldsymbol{\sigma}_{max}$). By contrast with the work presented in [53], we quantify the fractions of energy dissipated by micro-crack debonding, irreversible micro-crack opening and macro-fracture debonding.

3. FINITE ELEMENT DAMAGE MODEL

3.1. Calibration of the Continuum Damage model

We calibrated the DSID model against experimental stress/strain curves obtained during triaxial compression tests performed on Bakken shale samples using ConocoPhillips rock mechanics dataset [54]. We performed our simulation work on a range of triaxial tests from the different Bakken lithologies. However, for simplicity, we focus reporting on a set of results from a single representative suite of tests taken from the same depth and lithology, but at different levels of confinement (Sample B11 shown in Fig. 11). We used a MATLAB algorithm to minimize the squared residuals of the distance between experimental results y_i and numerical predictions $f(\boldsymbol{x}, \boldsymbol{B})$ as

$$S = \sum_{i=1}^{n} [y_i - f(\boldsymbol{x}, \boldsymbol{B})]^2 \tag{5}$$

Where $\boldsymbol{x}$ stands for the vector of known input variables (e.g., strain or stress, depending whether the load is controlled in force or displacement) and $\boldsymbol{B}$ is the vector of parameters that need to be calibrated. We employed the gradient method to minimize the difference between numerical and experimental stress-strain curves:

$$\boldsymbol{B}_{n+1} = \boldsymbol{B}_n - \gamma_n \Delta f(\boldsymbol{x}, \boldsymbol{B}) \tag{6}$$

γ_n is the step size; it varies from step to step. The algorithm was initialized with a reasonable initial vector $\boldsymbol{B}_0$, and with reasonable minimum and maximum values for the model parameters. Optimal DISD parameters (for S below a certain threshold value) are listed in Table II.

3.2. Cutting Plane algorithm

We adopt the cutting-plane algorithm [55] to implement the DSID model in ABAQUS FEM software. The purpose of the cutting plane algorithm, which belongs to the category of return mapping algorithms, is to ensure stable and convergent solutions with a reasonable simulation

time. The elastic predictor problem is solved with initial conditions which correspond to the converged values of the previous time step. A stress return correction is initiated if the trial elastic stress is outside of the yield surface. We follow the steps of the operator splitting theory [56] to obtain the incremental non-linear constitutive relationships that govern the DSID model:

Total	Elastic predictor	Return corrector
$\mathrm{d}\boldsymbol{\varepsilon} = \mathrm{d}\boldsymbol{\varepsilon}^E + \mathrm{d}\boldsymbol{\varepsilon}^{id}$	$\mathrm{d}\boldsymbol{\varepsilon} = \mathrm{d}\boldsymbol{\varepsilon}^E + \mathrm{d}\boldsymbol{\varepsilon}^{id}$	$\mathrm{d}\boldsymbol{\varepsilon} = 0$
$\mathrm{d}\boldsymbol{\sigma} = \mathbb{S}^{-1} : [\mathrm{d}\boldsymbol{\varepsilon}^E - \boldsymbol{\sigma} : \partial_{\boldsymbol{\Omega}}\mathbb{S} : \mathrm{d}\boldsymbol{\Omega}]$	$\mathrm{d}\boldsymbol{\sigma} = \mathbb{S}^{-1} : \mathrm{d}\boldsymbol{\varepsilon}$	$\mathrm{d}\boldsymbol{\sigma} = -\mathbb{S}^{-1} : [\mathrm{d}\boldsymbol{\varepsilon}^{id} + \boldsymbol{\sigma} : \partial_{\boldsymbol{\Omega}}\mathbb{S} : \mathrm{d}\boldsymbol{\Omega}]$
$\mathrm{d}\boldsymbol{\varepsilon}^{id} = \mathrm{d}\lambda\frac{\partial f_d}{\partial \boldsymbol{\sigma}}$	$\mathrm{d}\boldsymbol{\varepsilon}^{id} = 0$	$\mathrm{d}\boldsymbol{\varepsilon}^{id} = \mathrm{d}\lambda\frac{\partial f_d}{\partial \boldsymbol{\sigma}}$
$\mathrm{d}\boldsymbol{\Omega} = \mathrm{d}\lambda\frac{\partial g}{\partial \boldsymbol{Y}}$	$\mathrm{d}\boldsymbol{\Omega} = 0$	$\mathrm{d}\boldsymbol{\Omega} = \mathrm{d}\lambda\frac{\partial g}{\partial \boldsymbol{Y}}$

In the above equations, the total stress increment is obtained by differentiating the following constitutive relationship

$$\boldsymbol{\varepsilon}^E = \mathbb{S}(\boldsymbol{\Omega}) : \boldsymbol{\sigma} \tag{7}$$

as:

$$\mathrm{d}\boldsymbol{\varepsilon}^E = \mathbb{S}(\boldsymbol{\Omega}) : \mathrm{d}\boldsymbol{\sigma} + \boldsymbol{\sigma} : \partial_{\boldsymbol{\Omega}}\mathbb{S} : \mathrm{d}\boldsymbol{\Omega} \tag{8}$$

The return corrector can be rewritten as :

$$\frac{\mathrm{d}\boldsymbol{\sigma}}{\mathrm{d}\lambda} = -\mathbb{S}^{-1} : [\partial_{\boldsymbol{\sigma}} f_d + \boldsymbol{\sigma} : \partial_{\boldsymbol{\Omega}}\mathbb{S} : \partial_{\boldsymbol{Y}} g] \tag{9}$$

Equation 9 expresses the rate independent equation of stress relaxation (from a point outside of the yield surface to a point on the yield surface). Stress relaxation is calculated iteratively. The yield function is linearized around the current values of the state variables, $\boldsymbol{\sigma}_{n+1}^{(i)}$, $\boldsymbol{\Omega}_{n+1}^{(i)}$, as

$$f_{n+1}^{(i+1)} \approx f_{n+1}^{(i)} + \partial_{\boldsymbol{\sigma}} f_{n+1}^{(i)} : [\boldsymbol{\sigma}_{n+1}^{(i+1)} - \boldsymbol{\sigma}_{n+1}^{(i)}] + \partial_{\boldsymbol{\Omega}} f_{n+1}^{(i)} : [\boldsymbol{\Omega}_{n+1}^{(i+1)} - \boldsymbol{\Omega}_{n+1}^{(i)}] \tag{10}$$

After discretizing Equation 9 and the damage flow rule, we have:

$$\boldsymbol{\sigma}_{n+1}^{(i+1)} - \boldsymbol{\sigma}_{n+1}^{(i)} = -\Delta\lambda_{n+1}^{(i)}\mathbb{S}_{n+1}^{-1} : [\partial_{\boldsymbol{\sigma}} f_{n+1}^{(i)} + \boldsymbol{\sigma}_{n+1}^{(i)} : \partial_{\boldsymbol{\Omega}}\mathbb{S}_{n+1}^{(i)} : \partial_{\boldsymbol{Y}} g_{n+1}^{(i)}] \tag{11}$$

$$\boldsymbol{\Omega}_{n+1}^{(i+1)} - \boldsymbol{\Omega}_{n+1}^{(i)} = \Delta\lambda_{n+1}^{(i)}\partial_{\boldsymbol{Y}} g_{n+1}^{(i)} \tag{12}$$

After substituting Equation 11 in Equation 10, the Lagrange multiplier is calculated as:

$$\Delta\lambda_{n+1}^{(i)} = \frac{f_{n+1}^{(i)}}{\partial_{\boldsymbol{\sigma}} f_{n+1}^{(i)} : \mathbb{S}_{n+1}^{-1} : [\partial_{\boldsymbol{\sigma}} f_{n+1}^{(i)} + \boldsymbol{\sigma}_{n+1}^{(i)} : \partial_{\boldsymbol{\Omega}}\mathbb{S}_{n+1}^{(i)} : \partial_{\boldsymbol{Y}} g_{n+1}^{(i)}] - \partial_{\boldsymbol{\Omega}} f_{n+1}^{(i)} : \partial_{\boldsymbol{Y}} g_{n+1}^{(i)}} \tag{13}$$

Figure 4 shows the flow chart of the algorithm implemented in ABAQUS UMAT for the purpose of this study. Note that because the cutting-plane algorithm is based on a forward integration of the rate equations, it is not unconditionally stable. In order to validate and test the accuracy of the return mapping algorithm, we compared the results obtained with the cutting plane algorithm with those obtained with the direct secant algorithm (which we implemented in MATLAB). We simulated pure shear, uniaxial compression and uniaxial tension by applying strain loads of $\gamma_{12} = -2\%$, $\epsilon_{33} = -2\%$ and $\epsilon_{33} = 2\%$ respectively. All the other strain components were set to zero. We used 1,000 loading increments in the direct secant

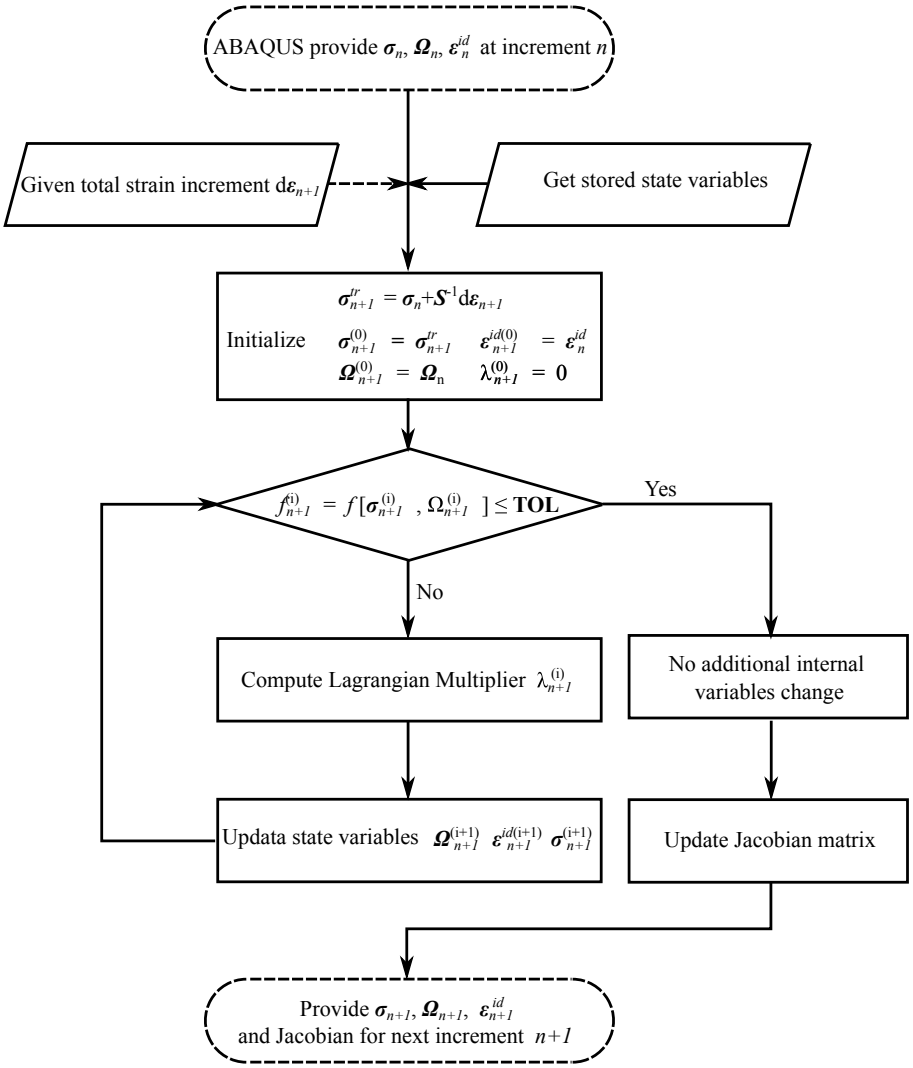

Figure 4. Cutting plane algorithm of the UMAT subroutine implemented in ABAQUS for the DSID model. Solid lines represent computational steps controlled by the programs written in UMAT. Dashed lines represent computational steps controlled by built-in subroutines of ABAQUS

algorithm. For the cutting plane algorithm, we compared the results obtained with MATLAB for 10, 100 and 1,000 loading increments, to the results obtained with ABAQUS for 50 loading increments applied in a one-element model.

Figure 5 shows the results. Note that higher loading increments ($\Delta\gamma$ or $\Delta\epsilon$) correspond to a lower number of increments. For all the cases simulated, the linear elastic response and non-linear damage part are well captured at the material point (MATLAB) and in the one-element (ABAQUS) simulations. The difference between the stress/strain curves obtained with the

direct secant method and with the cutting plane algorithm is less than 10% for a number of increments larger than 50 with the FEM, and larger than 100 with MATLAB. We conclude that the cutting plane algorithm is accurate for loading increments that are of the order of 0.01%. Moreover, the global FEM equation obtained after assembling all the elementary matrix equations obtained with the UMAT subroutine was solved with the 'standard solver' built in ABAQUS, which is based on an unconditionnally stable algorithm.

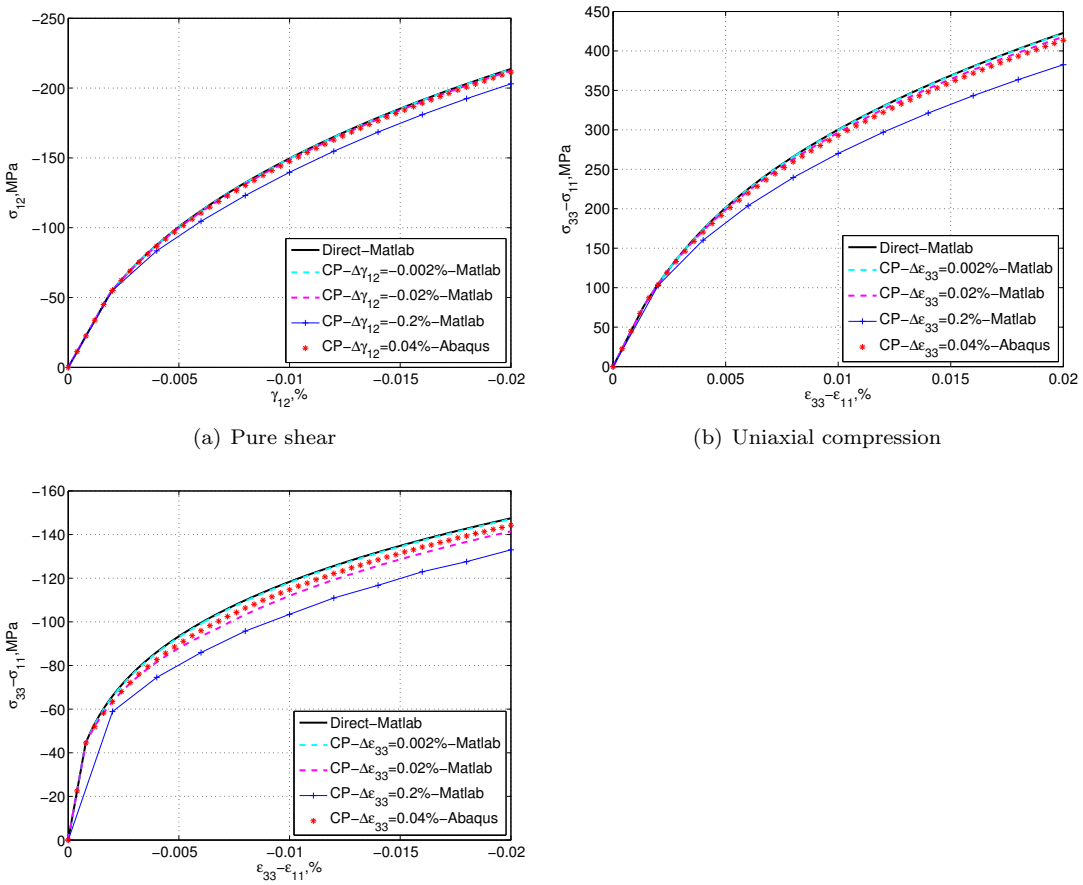

(a) Pure shear

(b) Uniaxial compression

(c) Uniaxial tension

Figure 5. Verification and accuracy tests. Comparison of the stress/strain curves predicted by the cutting plane (CP) algorithm (one-element tests performed with ABAQUS and material point tests performed in MATLAB) and by the direct secant algorithm (material point tests performed in MATLAB). The total loading was 2% in all tests; several loading increments were tested.

4. CALIBRATION OF THE COHESIVE ZONE MODEL

The objective of this paper is to couple the DSID model to a CZM to predict continuum damage propagation before and after shear localization. In the following, we propose a calibration method that couples the propagation of micro-cracks (DSID model) to that of macro-fractures (CZM) in mode II. We use a bilinear CZM, which depends on three constitutive parameters: the cohesive (shear) stiffness K_0, the cohesive (shear) strength τ_{max} and the energy release rate G_{IIc} (in mode II). Based on a sensitivity analysis of τ_{max} and G_{IIc}, we introduce a relationship to account for the dependence of the cohesive zone failure to the confining pressure. In the following, the procedure to determine the material parameters of the CZM is explained. We calibrate the CZM against the same experimental dataset as the one used to calibrate the DSID model assigned to the Finite Elements. This calibration stage is required to ensure that multi-scale crack propagation is modeled as the transition between damage propagation without and with discrete fracture, within the same material - as opposed to the coupled activation of fracture propagation in a composite made of a weak layer (CZM) embedded in a brittle continuum (CDM).

4.1. Choice of the cohesive stiffness: numerical requirements

In the Finite Element Method, it is assumed that a Cohesive Zone has a zero-thickness. The stiffness of CZM elements is chosen so as to ensure that the effective stiffness of a laminated material modeled with a Cohesive Zone of finite thickness is not influenced by the stiffness of this Cohesive Zone (in other words, the stiffness of the bulk material in the laminated composite is negligible in front of that of the cohesive elements) [57]. Figure 6 shows how the CZM influences the deformation of a sandwich laminate. Assuming that shear stress is uniformly distributed in the cohesive zone and in the bulk of the bounding material, we have:

$$\begin{aligned} \tau &= G\gamma = K_0\Delta \\ \gamma_{eff} &= \frac{2\delta t + \Delta}{2\,t} = \gamma + \frac{\Delta}{2t} \end{aligned} \tag{14}$$

Where τ is the shear stress, γ_{eff} is the effective shear strain of the sandwich laminate element, $\gamma = \frac{\delta t}{t}$ is the shear strain of one of the two bounding layers and K_0 represents the cohesive stiffness that relates the cohesive shear with the shear displacement Δ. The equilibrium $\tau = G_{eff}\gamma_{eff}$ condition requires that the effective shear modulus satisfies:

$$G_{eff} = G(\frac{1}{1 + \frac{G}{2K_0\,t}}) \tag{15}$$

Given that the cohesive stiffness should not influence the effective modulus of composite, the cohesive shear stiffness must satisfy $G << 2K_0\,t$. Numerically, the CZM is assigned a stiffness expressed as:

$$K_0 = \frac{\alpha\,G}{t} \tag{16}$$

With $\alpha >> 1$. In theory, K_0 should be infinite to insure that all the elastic deformation energy is stored in the bulk material and not in the cohesive zone prior to debonding (equation 4). However, oscillations were noted for very high values of α [57]. We choose $\frac{\alpha}{t} = 50$ for all the following simulations, which ensures that the elastic energy stored in the cohesive zone prior

to debonding is insignificant compared to the total energy release G_c that is dissipated after total debonding. Note that according to the derivations above, the CZM stiffness does not depend on the loading path, and thus does not depend on the confining stress.

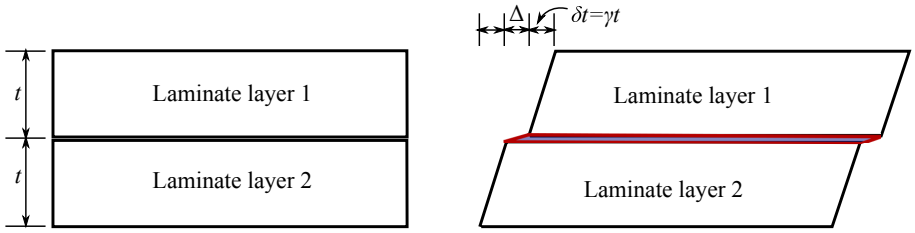

Figure 6. Influence of the stiffness of a cohesive zone in a numerical model of laminated material, modified from [57].

4.2. Determination of the cohesive strength: critical damage value

The cohesive strength is distinct from the stress threshold necessary to trigger damage. In order to capture the energy flow between the damaged continuum and the material surfaces of the cohesive zone [51, 53], we define the cohesive strength as the stress that marks the transition between smeared micro-cracking (accounted for by the DSID model implemented in Finite Elements) and discrete macro-cracking (accounted for by the CZM). Our usage of cohesive strength also differs from conventional CZM models (without matrix damage) where the term refers to the material's peak strength. Accordingly, we determine the critical continuum damage value (i.e. micro-crack density) above which micro-crack interaction cannot be neglected, and we calculate the shear stress necessary to reach this critical damage value in mode II. In order to determine the critical damage value, we calculate the damaged shear modulus of a 2D REV that contains one set of parallel equally sized cracks, using two methods: first, the DSID model, which does not account for micro-crack interaction; second,Kachanov's micro-mechanical model [58], which accounts for micro-crack interaction. The difference between the shear modulus calculated with Kachanov's model and the shear modulus calculated with the DSID model increases with damage, because micro-crack interactions increase with damage. The critical damage value is defined as the level of damage above which the difference between Kachanov's shear modulus and the DSID shear modulus stops increasing. Note that in the DSID model, the damage tensor is a phenomenological variable, which is not equal to the micro-crack density defined by Kachanov. Both damage variables account for meso-scale crack development and stiffness degradation. In the following, we start by recalling the main equations of Kachanov's micro-mechanical damage model (for the sake of completeness) and we then explain in detail an original method to determine the critical damage value, which marks the transition from CDM to CZM.

4.2.1. Kachanov's micro-mechanical model. In the 2D micro-mechanical damage model proposed by Kachanov, the stress and strain fields in a linear elastic plate containing N cracks subjected to the stress $\boldsymbol{\sigma}^{\infty}$ at infinity are calculated as those in a plate subjected to zero far field stress and containing N loaded micro-cracks. The faces of each micro-crack ($i = 1, ..., N$) are subjected to the traction $\boldsymbol{t}_i^0 = \boldsymbol{n}_i \cdot \boldsymbol{\sigma}^{\infty}$, in which $\boldsymbol{n}_i$ is the unit vector normal to the

faces of the $i-th$ crack. According to the superposition theory for elastic media, this problem can be solved by considering N plates containing only one crack subjected to the traction $\boldsymbol{t}_i$ $(i = 1, ..., N)$, defined as the sum of $\boldsymbol{t}_i^0$ and the additional tractions due to stress interactions with the other micro-cracks. The tractions can be determined by solving a system of integral equations, as follows [58]:

$$\boldsymbol{t}_i(\zeta_i) = \boldsymbol{t}_i^0 + \boldsymbol{n}_i \cdot \sum_{j \neq i} \int_{-l_j}^{l_j} \boldsymbol{\sigma}_j^n(\zeta_i, \zeta_j)[\boldsymbol{n}_j \cdot \boldsymbol{t}_j(\zeta_j)] + \boldsymbol{\sigma}_j^\tau(\zeta_i, \zeta_j)[\boldsymbol{\tau}_j \cdot \boldsymbol{t}_j(\zeta_j)] d\zeta_j \tag{17}$$

In which l_j is the half length of the $j-th$ crack and $\boldsymbol{\tau}_j$ is the unit vector that is tangential to the faces of the $j-th$ crack. $\boldsymbol{\sigma}_j^n(\zeta_i, \zeta_j)$ (respectively $\boldsymbol{\sigma}_j^\tau(\zeta_i, \zeta_j)$) is the stress tensor at the current point ζ_i on the $i-th$ crack, generated by a pair of equal and opposite unit forces located at point ζ_j along the normal (respectively tangential) direction of the $j-th$ crack. Following the approximation proposed and validated by Kachanov [58], we consider that the stress applied at the $i-th$ crack is that due to the traction applied at infinity and the average tractions along the faces of the $j-th$ cracks. In other words, we assume that the stress at ζ_j is not sensitive to the deviations of $\boldsymbol{t}_j(\zeta_j)$ from the average $\langle \boldsymbol{t}_j \rangle$. This allows transforming equation 17 into:

$$\boldsymbol{t}_i(\zeta_i) = \boldsymbol{t}_i^0 + \langle \boldsymbol{n}_j \cdot \boldsymbol{t}_j(\zeta_j) \rangle \, \boldsymbol{n}_i \cdot \sum_{j \neq i} \overline{\boldsymbol{\sigma}}_{\boldsymbol{j}}^{\boldsymbol{n}}(\zeta_i) + \langle \boldsymbol{\tau}_j \cdot \boldsymbol{t}_j(\zeta_j) \rangle \, \boldsymbol{n}_i \cdot \sum_{j \neq i} \overline{\boldsymbol{\sigma}}_{\boldsymbol{j}}^{\boldsymbol{\tau}}(\zeta_i) \tag{18}$$

In which:

$$\langle \boldsymbol{n}_j \cdot \boldsymbol{t}_j(\zeta_j) \rangle = \int_{-l_j}^{l_j} \boldsymbol{n}_j \cdot \boldsymbol{t}_j(\zeta_j) d\zeta_j \tag{19}$$

$$\langle \boldsymbol{\tau}_j \cdot \boldsymbol{t}_j(\zeta_j) \rangle = \int_{-l_j}^{l_j} \boldsymbol{\tau}_j \cdot \boldsymbol{t}_j(\zeta_j) d\zeta_j \tag{20}$$

$$\overline{\boldsymbol{\sigma}}_{\boldsymbol{j}}^{\boldsymbol{n}}(\zeta_i) = \int_{-l_j}^{l_j} \boldsymbol{\sigma}_j^n(\zeta_i, \zeta_j) d\zeta_j \tag{21}$$

$$\overline{\boldsymbol{\sigma}}_{\boldsymbol{j}}^{\boldsymbol{\tau}}(\zeta_i) = \int_{-l_j}^{l_j} \boldsymbol{\sigma}_j^\tau(\zeta_i, \zeta_j) d\zeta_j \tag{22}$$

$$\tag{23}$$

$\overline{\boldsymbol{\sigma}}_{\boldsymbol{j}}^{\boldsymbol{n}}(\zeta_i)$ is the stress generated at point ζ_i due to a uniform tensile load of unit intensity applied in the direction normal to the faces of the $j-th$ crack. Noting $x = \tau_j$ and $y = n_j$, we have [58]:

$$\begin{aligned} \sigma_{xx}^n &= I_2 - 8y^2 I_4 + 8y^4 I_6 \\ \sigma_{xy}^n &= 2(-yI_3 + xyI_4 + 4y^3 I_5 - 4xy^3 I_6) \\ \sigma_{yy}^n &= I_2 + 4y^2 I_4 - 8y^4 I_6 \end{aligned} \tag{24}$$

Note that in the last of the above equations, we corrected a typo in the equations presented in [58]. $\overline{\boldsymbol{\sigma}}_{\boldsymbol{j}}^{\boldsymbol{\tau}}(\zeta_i)$ is the stress generated at point ζ_i due to a uniform tensile load of unit intensity applied in the direction tangential to the faces of the $j-th$ crack. Noting $x = \tau_j$ and $y = n_j$,

we have [58]:

$$\begin{aligned}\sigma_{xx} &= 2(3yI_3 - 3xyI_4 - 4y^3I_5 + 4xy^3I_6)\\ \sigma_{xy} &= I_2 - 8y^2I_4 + 8y^4I_6\\ \sigma_{yy} &= 2(-3yI_3 + xyI_4 + 4y^3I_5 - 4xy^3I_6)\end{aligned} \tag{25}$$

In which:

$I_1 = 4l^3 \frac{\sqrt{\gamma}-\sqrt{\alpha}}{\sqrt{\delta}(\sqrt{\alpha}+\sqrt{\gamma}+\sqrt{\delta})^2}$
$I_2 = 4l^2 \frac{1}{\sqrt{\delta}(\sqrt{\alpha}+\sqrt{\gamma}+\sqrt{\delta})}$
$I_3 = 2l^3 \frac{\sqrt{\gamma}-\sqrt{\alpha}}{(\alpha\gamma)^{1/2}\delta^{3/2}}$
$I_4 = 2l^2 \frac{\sqrt{\gamma}+\sqrt{\alpha}}{(\alpha\gamma)^{1/2}\delta^{3/2}}$
$I_5 = \frac{l^3}{2} \frac{3\sqrt{\alpha\gamma}(\sqrt{\gamma}+\sqrt{\alpha})^2(\sqrt{\gamma}-\sqrt{\alpha})+\delta(\gamma^{3/2}-\alpha^{3/2})}{(\alpha\gamma)^{3/2}\delta^{5/2}}$
$I_6 = \frac{l^2}{2} \frac{3\sqrt{\alpha\gamma}(\sqrt{\gamma}+\sqrt{\alpha})^3+\delta(\gamma^{3/2}+\alpha^{3/2})}{(\alpha\gamma)^{3/2}\delta^{5/2}}$
$\alpha = (x-l)^2 + y^2$
$\beta = 2(x^2 + y^2 - l^2)$
$\gamma = (x+l)^2 + y^2$
$\delta = \beta + 2\sqrt{\alpha\gamma}$

Equations 17 allow solving for the tractions $\boldsymbol{t}_i(\zeta_i)$. The average relative displacement vector $< \boldsymbol{b}_i >$ across the faces of the $i-th$ crack is found by superposing the displacements due to punctual tractions at each point of the $i-th$ crack faces [58]:

$$< \boldsymbol{b}_i >= \frac{4l_i}{E_0} \int_{-l_i}^{l_i} \boldsymbol{t}_i(\zeta_i)[1 - (\zeta_i/l_i)^2]^{1/2} d\zeta_i \tag{26}$$

In which E_0 is the Young's modulus of the matrix (bounding material) between the cracks. The fourth order effective compliance tensor $\mathbb{S}^{eff}$ is used to relate the average strain $< \boldsymbol{\epsilon} >$ to the applied far field stress $\boldsymbol{\sigma}^{\infty}$ over a representative area A:

$$< \boldsymbol{\epsilon} >= \mathbb{S}^{eff} : \boldsymbol{\sigma}^{\infty} = \mathbb{S}^{0} : \boldsymbol{\sigma}^{\infty} + \frac{1}{2A} \sum_{i=1}^{N} \int_{-l_i}^{l_i} [\boldsymbol{n}_i(\zeta_i)\boldsymbol{b}_i(\zeta_i) + \boldsymbol{b}_i(\zeta_i)\boldsymbol{n}_i(\zeta_i)] d\zeta_i \tag{27}$$

Where $\mathbb{S}^0$ is elastic compliance tensor without cracks, and $\boldsymbol{n}_i(\zeta_i)$ is the unit vector normal to the $i-th$ crack face at point ζ_i. We consider flat cracks, for which $\boldsymbol{n}_i(\zeta_i)$ is a constant. Equation 27 thus becomes:

$$< \boldsymbol{\epsilon} >= \mathbb{S}^{0} : \boldsymbol{\sigma}^{\infty} + \frac{l_i}{A} \sum_{i=1}^{N} [\boldsymbol{n}_i < \boldsymbol{b}_i > + < \boldsymbol{b}_i > \boldsymbol{n}_i] \tag{28}$$

The expressions of the stress distributions that are involved in the integral terms of Equations 17 and 26 are very complex, which makes it challenging to obtain the exact solution of the traction and displacement distributions along each crack face. To overcome this problem, several approximation methods were proposed [58, 59, 60, 61]. In the following, we adopt Kachanov's approximation method [58], in which equation 26 is written as follows:

$$< \boldsymbol{b}_i >= \frac{\pi\, l_i}{E_0} < \boldsymbol{t}_i > \tag{29}$$

Where $< \boldsymbol{t}_i >$ is the mean traction field that applies to the $i-th$ crack.

4.2.2. Critical continuum damage value. In the following, we consider a 2D REV that contains cracks perpendicular to the x-axis, and we calculate the shear modulus in the xy-direction. Stress interactions between micro-cracks are highly dependent on the position of these cracks, i.e. the crack pattern has a major effect on the overall mechanical response of the REV. Hence, in order to determine the critical damage value above which the damaged elasticity tensor predicted by the DSID model departs from the damaged elasticity tensor expected with crack interactions, we tested several crack patterns (Figure 7), denoted as: "parallel" (alined crack centers), "zigzag" (crack centers in staggered rows), "random" (crack centers positioned according to a random space distribution) and "special case" (random distribution of centers with no cracks close to the boundary).

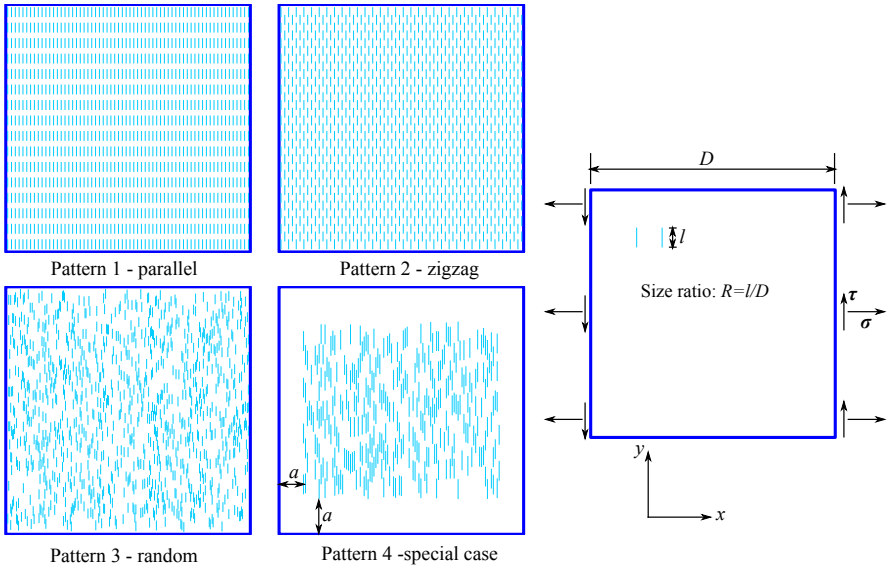

Figure 7. Crack patterns used to compare the damaged shear modulus according to the DSID model and according to Kachanov's micro-mechanics model

Two sets of simulations are performed, with REV sizes equal to 10 and 25 times that of the cracks. The crack density ρ is defined as:

$$\rho = \frac{1}{A}\sum_{i=1}^{N} l_i^2 \tag{30}$$

In the present case, because all the cracks are perpendicular to x-axis, the elastic moduli are affected by the crack density (ρ) in Kachanov's model, and by the $xx-$ component of the damage tensor (Ω_{xx}) in the DSID model. We simulated the pure shear test at the material point with the DSID model, and we used Equation 31 to calculate the effective shear modulus along the xy-direction (solid black line in Figure 8). The shear modulus was obtained from the

compliance tensor:

$$\mathbb{S} = \frac{\partial^2 G_s}{\partial \boldsymbol{\sigma}^2}. \tag{31}$$

Where G_s is Gibbs free energy expressed in Table I. We calculated the damaged elastic tensor with Kachanov's model for several values of crack density, by either increasing the number of cracks in the REV with a fixed crack length (crack initiation), or by increasing the length of a fixed number of cracks in the REV (crack propagation). Note that in all simulations, the centers of the cracks were randomly distributed inside the REV, with non-overlap and non-intersection constraints.

We observe that in the micro-mechanical model, the evolution rate of the shear modulus with damage depends on the crack pattern considered (dashed lines in Figure 8). Overall, the evolution rate of the shear modulus with damage is higher in the DSID model than in the micro-mechanical model, which accounts for the shielding effects of interacting micro-cracks. It is worth noting that for a given crack pattern though, the value of the damaged shear modulus only depends on crack density - and not on the type of damage growth (crack initiation vs. crack propagation). Results also show that the lowest (respectively highest) values of damaged shear modulus are obtained for the "parallel" pattern (respectively "zigzag" pattern). In nature, crack patterns are not periodic in rocks, therefore we considered a random distribution of crack centers. In order to assess boundary effects, we compared the "random" pattern to the "special case", and found that removing cracks from the area close to the boundary did not change the results significantly neither for the model of crack initiation or for the model of crack propagation. Therefore we did not plot the results obtained with the "special case" in Figure 8. In the following, we base our calibration on the "random" pattern (pattern 3). Kachanov [59] found that crack interaction could not be neglected for crack densities that exceed $\rho = 0.3$. We note a 20% relative difference between the damaged shear modulus predicted by the DSID model for $\Omega_{xx} = 0.3$ and that predicted by the micro-mechanical model for a density of randomly distributed cracks equal to $\rho = 0.3$. Although this difference is partly due to the distinct mathematical definitions used for ρ and Ω_{xx}, the rate of shear modulus degradation is mainly controlled by the interaction or non-interaction between cracks. The relative difference in shear modulus does not change any further when the damage density ρ or the damage component Ω_{xx} increases beyond 0.3. Thus, in the following, we consider that the relative difference of 20% is a representative deviation to mark the transition between continuum damage and discrete fracture, and we set the critical damage value as $\Omega_{xx} = 0.3$ in mode II. To summarize, the value of 0.3 is not an absolute theoretical limit, but rather the approximate point where micromechanical behaviors transition from being dominantly related to microcrack nucleation to including nonlinear effects caused by microcrack propagation.

4.2.3. Cohesive shear strength under various confining pressures. In our model, the transition between damage propagation without and with discrete fracture (i.e., before and after shear localization) is determined by the continuum damage value calibrated above. The cohesive strength of the CZM is the shear stress at which this critical damage value is reached, which varies with the boundary conditions - the confining pressure in particular. In the following, we establish a relationship between the CZM cohesive shear strength τ_{max} and the confining pressure, which will allow determining the critical energy release rate G_{IIc} in the last part of the calibration. We simulated a confined shear test at the material point with the DSID model by applying a hydrostatic confining pressure followed by a shear stress. The shear

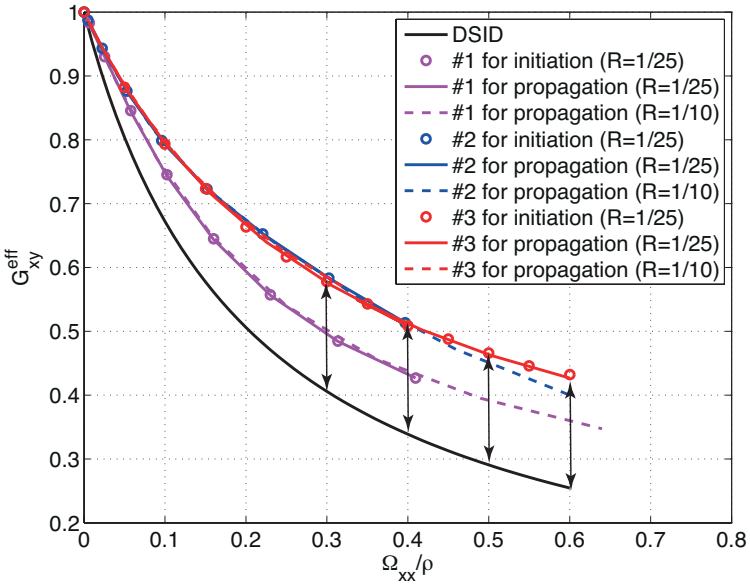

Figure 8. Damaged shear modulus calculated with the DSID model and with Kachanov's micro-mechanical model for a set of cracks parallel to the x-axis, for various crack patterns. Damage propagation is modeled by increasing the length l of a fixed number of equally sized cracks that are randomly distributed in the REV of size D, from $R = l/D = 0$ to $R = l/D = 1/25$ or from $R = l/D = 0$ to $R = l/D = 1/10$. Damage initiation is modeled by increasing the number of equally sized cracks that are randomly distributed in the REV (with either $R = 1/10$ or $R = 1/25$).

loading was stopped when damage in the direction perpendicular to the shear direction reached 30% (i.e., $\Omega_{xx} = 0.3$). The loading paths followed those of the laboratory experiments used for calibration. For hydrostatic confining pressures of 6.9MPa (1000psi), 13.8MPa (2000psi), 20.7MPa (3000psi) and 27.6MPa (4000psi), we found that the shear stress needed to reach $\Omega_{xx} = 0.3$ was τ_{max} =81.4MPa, 86.1MPa, 91.2MPa and 96.6MPa respectively (Figure 9). We note that when $\Omega_{xx} = 0.3$, the damage component perpendicular to the shear plane (Ω_{zz}) is higher for higher confining stresses.

4.3. Determination of the cohesive energy release rate

After the cohesive strength (defined here as the transition between micro- and macro-scale propagation) is reached, both the cohesive element and the bounding material near the cohesive segment $[\delta_0; \delta_f]$ begin to unload (Figure 10). The elastic energy E_e stored in the bounding material located in this area flows into cohesive elements and is transformed into dissipated cohesive energy E_c (see Equation 4). Note that due to stress concentrations, only the elements that are along the fracture faces reach the cohesive strength. As the energy is released from the continuum to the fracture faces, the other elements along the fracture faces start unloading.

Following the approach used by Woelke et al [23] and Paulino [24], we calibrated the value of the cohesive shear energy release rate G_{IIc} by matching a pre-assumed value of G_{IIc} with the energy released during a confined axial compression test conducted in ConocoPhillips rock

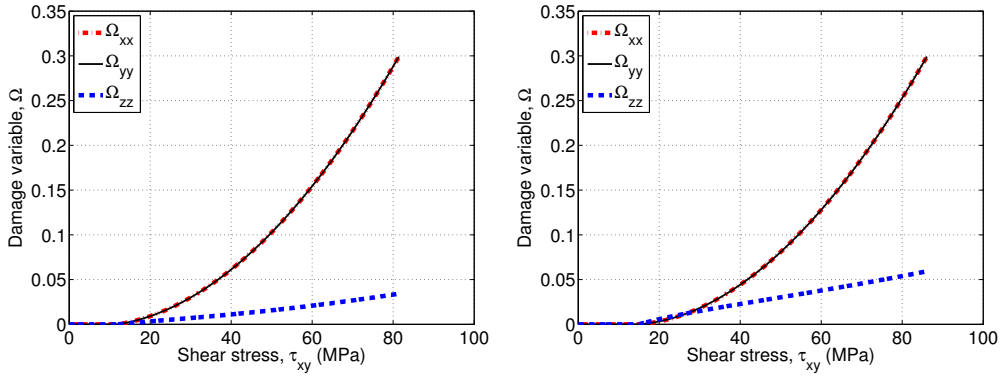

(a) Confining pressure $=6.9MPa$ (b) Confining pressure $=13.8MPa$

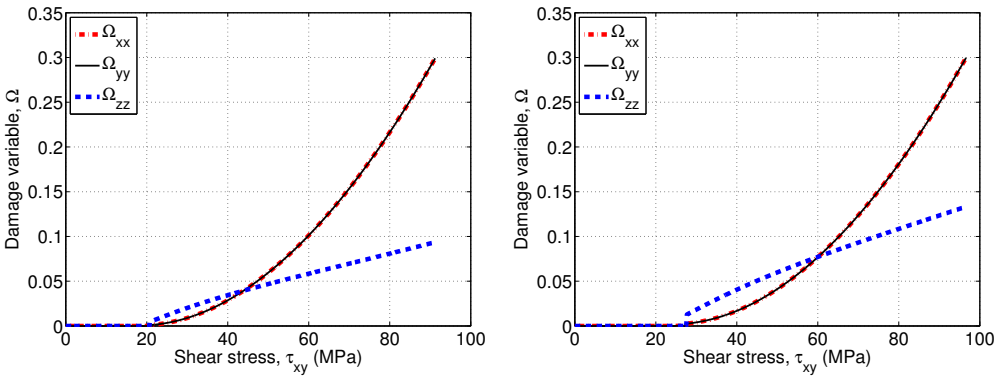

(c) Confining pressure $=20.7MPa$ (d) Confining pressure $=27.6MPa$

Figure 9. Material Point simulation of a confined shear test (pure mode II) with the DSID model, up to the critical damage value (which marks the transition with the opening of the cohesive zone).

mechanics laboratory. Typical shear failure planes that were observed in many of the Bakken shale plugs after triaxial compression tests are shown for sample B11-3, in Figure 11. In order to simulate the transition from micro-scale continuum damage to macro-scale cohesive zone propagation, we modeled cylindrical plugs with the same dimensions as those tested in the laboratory: diameter 25.4mm (1 inch) and length 50.8mm (2 inches). We modeled the planes of weakness observed experimentally by single two-dimensional planar cohesive zone. We used a pure mode II CZM, even though the triaxial compression tests do not lead to a pure mode II failure. Indeed it should be noted that some of the plugs from other samples failed in a more irregular three-dimensional fracture pattern. For the more complex cases the cohesive method can still be used; however, modeling branching cohesive zones is outside the present scope. In order to avoid convergence issues associated with triangular elements in the cohesive zone, we modeled the cohesive zone as a diagonal plane placed with a slight offset (Δ) from the top and bottom of the sample, as shown in Figure 12. This geometric choice allowed us meshing the Finite Element domain with brick elements, which were projected into rectangular cohesive

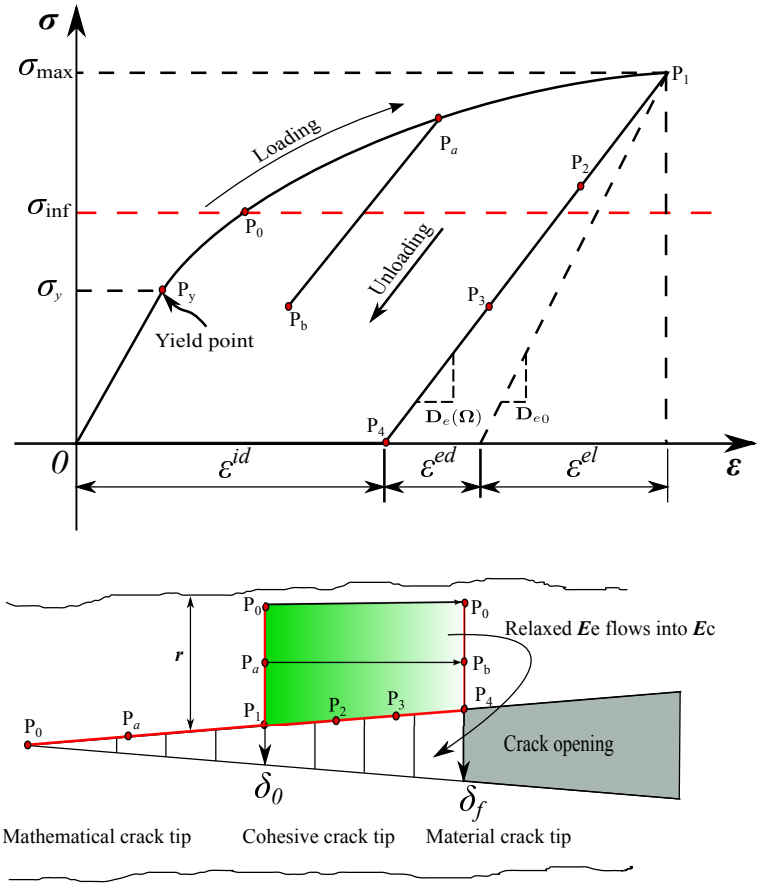

Figure 10. Evolution of the stress/strain state in the damaged zone as a cohesive fracture propagates. Note that the displacements and deformation increments that would be obtained in mode II are challenging to sketch, therefore we illustrate the energy flow model in mode I. Note that the principle is the same in mode II. Different material points in the bounding material (green shaded area) are subjected to different stress and damage states. Continuum damage initiates at P_y, ahead of the fracture tip. P_0 indicates a damaged state at a material point along the cohesive zone, for which stress is less than the cohesive strength. P_0-P_a-P_1 illustrates the stress build-up along the cohesive zone, as the material point gets closer to the tip. P_1 marks the material point at the boundary between the bounding material and the cohesive zone for which shear stress reaches the cohesive shear strength: the cohesive zone starts to open. P_1-P_2-P_3-P_4 illustrates the progressive unloading of the bounding material from the cohesive crack tip (debonding initiation) to the material crack tip (complete debonding). The path P_0-P_a-P_b illustrates the transfer of energy from the damaged elastic bounding material to the crack faces. Within the damaged zone, the bounding material closer to the material crack tip is subjected to unloading (P_a to P_b). At a distance larger than r away from the damaged zone, the bounding material stress state is not influenced by the cohesive crack (P_0 remains at P_0 whatever the location of the material point is along the crack).

elements. We performed the tests for a ratio of offset / sample length equal to $\Delta/L = 1/10$ and $\Delta/L = 1/40$, and verified that the stress/strain curve predicted numerically was not sensitive to the offset. In the following simulations, we used $\Delta/L = 1/40$.

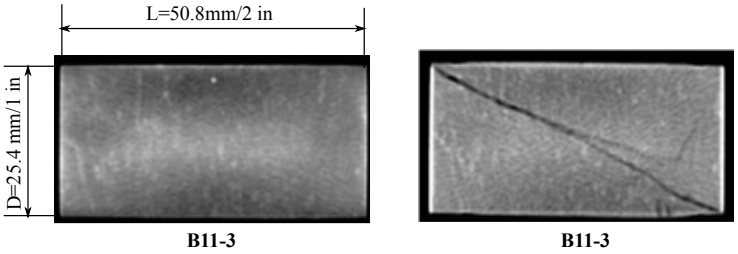

Figure 11. Pictures of Bakken shale samples before (left) and after (right) the triaxial compression test leading to mode II failure.

In the experiments, friction between the sample and the loading plates is an inevitable source of some of the plug damage, but it is difficult to parameterize. Therefore we assumed that Finite Elements representing the platens and those representing the rock in contact with the platens shared the same nodes. The bounding steel platens were idealized as stiff 2.5mm plates. For steel finite elements, we assumed a linear elastic behavior with $E = 200GPa$ and $\nu = 0.3$. For shale finite elements, we used the DSID model calibrated against triaxial compression tests (Table II).

During the simulation, we approximated the laboratory loading conditions by fixing the 6 degrees of freedom of the center point in the bottom steel plate to prevent free body movement. During the first stage of the simulation, we applied the confining pressure at the top and lateral surfaces of the shale sample. Then we applied an axial displacement boundary condition at the top face of the top steel plate.

Figure 12 shows the distribution of horizontal damage components $\mathbf{\Omega}_{xx} = \Omega_{11}$ and $\mathbf{\Omega}_{yy} = \Omega_{22}$, which represent vertical micro-crack planes (normal to the x_1 and x_2 axes) in the upper half of the sample, just after complete failure. The confining pressure was 13.8 MPa and the top surface was subjected to a uniform quasi-static loading to represent experiments performed with an axial strain rate of $10^{-5}s^{-1}$. The cumulated displacement at the end of the simulation was 0.708mm. We note that the two horizontal damage components are distributed uniformly in the sample, where $\mathbf{\Omega}_{xx} = \mathbf{\Omega}_{yy} = 0.15$, or about 15% stiffness degradation at the point macroscopic failure, except close to the steel plate. Figure 13 shows the corresponding axial stress distribution at the end of the simulation, just after failure. The same boundary effects were noted close the steel plate elements. In order to verify the absence of mesh dependency of the model, we performed the simulation with three different mesh sizes, in which the whole Finite Element domain was meshed with 5,100 elements (coarse mesh); 11,400 elements (intermediate); and 23,200 elements (fine). For the same confining pressure and vertical displacement imposed at the top plate, stress distributions were very similar in the three FE models, except at the interface between the plates and rock sample. Figure 14 shows the shear stress distribution along the weak plane modeled with the fine cohesive zone just before failure, when the vertical displacement of the top steel plate is 0.652mm. Note that at this stage, the shear stress in all the cohesive elements have entered the softening regime,

therefore shear stress is less than the cohesive shear strength. Shear stress relaxation occurred first at the top and bottom. Thus the model captures failure localization as observed in the experiments, with an initiation of the debonding close to the steel plates.

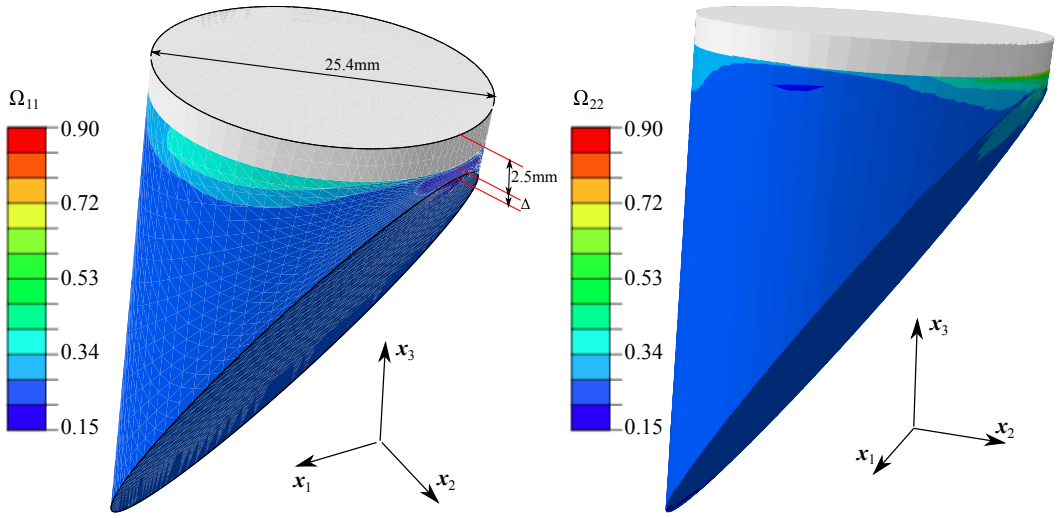

Figure 12. Left/right: horizontal/vertical damage (i.e. distribution of vertical/horizontal micro-crack planes, normal to the x_1/x_2 axis) just after failure subsequent to a triaxial compression test (upper half of the shale sample). The applied confining pressure was 13.8 MPa and the total displacement imposed at the top surface was 0.708mm.

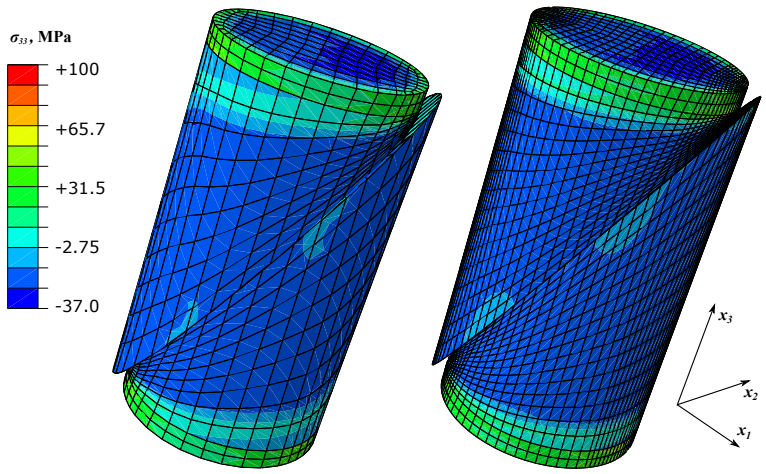

Figure 13. Distribution of axial stress just after failure subsequent to a triaxial compression test with the coarse (5,100 elements) and fine (23,200 elements) meshes. The applied confining pressure was 13.8 MPa and the total displacement imposed at the top surface was 0.708mm. Note that the displacements were amplified 5 times, and compressive stress was counted negative.

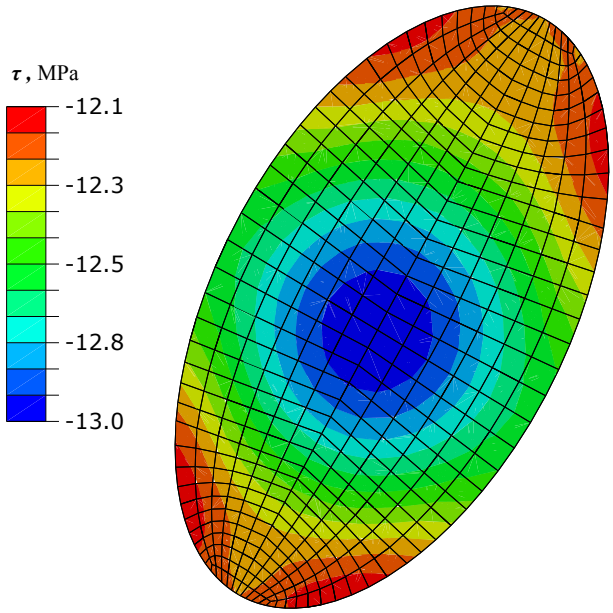

Figure 14. Shear stress distribution calculated in the cohesive zone after the initiation of debonding and before the total failure subsequent to a triaxial compression test, with the fine mesh (23,200 elements). The confining pressure was p_c =13.8 MPa and the total displacement imposed at the top surface was 0.652mm.

After the simulation, we extracted the mean axial stress and average displacement of the top steel plate. The differential stress was obtained by subtracting the corresponding confining pressure out of the mean stress, and the axial strain was obtained by dividing the mean displacement with sample length and subtracting the initial strain due to confining pressure. We calibrated the parameters against the stress/strain curve of sample B11-3, under a 13.8 MPa confinement pressure. Figure 15 shows a range of simulated stress/strain curves varying minor numerical parameters against several other of the Bakken sample tests run at the same confinement. The results show that the calibrated simulated curves fall within the range of the rock mechanics tests, showing a good match to the overall deformation response of the suite of laboratory samples. In order to capture the specific variability of each test, calibrated parameters would need to be derived independently. In reality, each of the Bakken shale plugs reflects some lithologic variability, as revealed by XRD data (not discussed here). We tried several values of cohesive shear energy release rate (G_{IIc}) until we were able to capture the post-peak behavior with enough accuracy. Note that the peak of differential stress corresponds to the cohesive strength that marks the transition between smeared damage propagation and discrete fracture propagation. The bilinear cohesive model captures the softening behavior, especially at low confining pressure. As can be seen in Figure 15(b), simulations performed with three different mesh sizes provide similar results, which shows that the proposed computational framework is mesh independent. It is also noted that the offset distance Δ has no significant influence on the post-peak behavior (Figure 15(c)).

The energy required to produce shear displacements increases with the normal stress

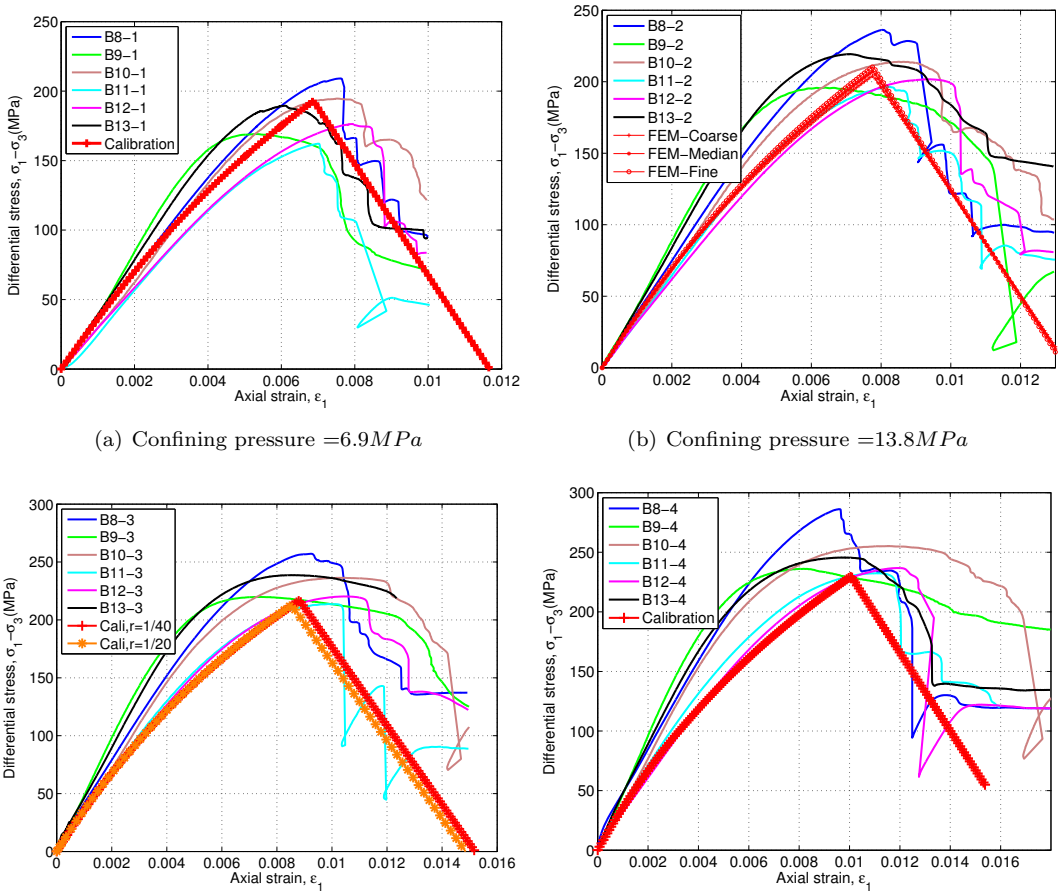

(a) Confining pressure =6.9MPa

(b) Confining pressure =13.8MPa

(c) Confining pressure =20.7MPa

(d) Confining pressure =27.6MPa

Figure 15. Experimental and numerical stress/strain curves obtained during triaxial tests under various confining pressures. Note: samples B8-B13 correspond to different lithologies, which results in different stress/strain curves. For p_c = 13.8MPa, mesh dependency was investigated by using a fine (5,100 elements), intermediate (11,400) and fine (23,200 elements) meshes. For p_c = 20.7MPa, the sensitivity of the model to the offset effects was investigated by using two ratios of offset / sample length: $r = \Delta/L = 1/20$ and $r = \Delta/L = 1/40$. Note that by construction, the adopted cohesive zone model cannot capture the residual stress after failure. This phenomenon, due to friction at fracture faces, would require additional parameters and a more sophisticated CZM (e.g., [62]).

that applies on the faces of the cohesive zone, therefore the cohesive shear energy release rate increases with the confining pressure. Figure 16 compares the empirical relationship between simulated confining pressure and cohesive shear strength for the CDM (red axis) or cohesive shear energy release rate CZM (black axis) domains. We plotted the four previously calibrated cohesive shear strengths τ_{max} against confining pressure p_c, and interpolated a linear relationship between cohesive shear strength and confining pressure (red line). We simulated seven additional pure shear tests at the material point (red circles in Figure 16) for confining pressures in the range $0 - 30MPa$. For each of these additional tests, we calculated the cohesive shear strength as the shear stress necessary to reach a horizontal damage of 30% in the bounding material represented by the DSID model. It is verified that the cohesive shear strength obtained in the additional tests followed the linear relationship obtained by interpolation. A linear relationship was also interpolated between the cohesive strength τ_{max} and the cohesive shear energy release rate G_{IIc} obtained in the CZM calibration procedure (blue squares in Figure 16). Consequently, we adapted the bilinear CZM to account for the dependence of the shear strength τ_{max} and energy release rate G_{IIc} to the confining pressure, as shown in Figure 17. The modified failure envelope conforms better to experimental observations,which indicate that the deviatoric stress necessary to initiate fracture propagation and the subsequent energy release rate G_{IIc} both depend on the stress normal to fracture faces, the loading strain rate and temperature. Like in previous models of frictional CZMs [62], we only considered quasi-static loading conditions and we ignored thermal effects. In the following simulations of fracture propagation with process zone, we used the failure envelope shown in Figure 17 to determine the CZM properties.

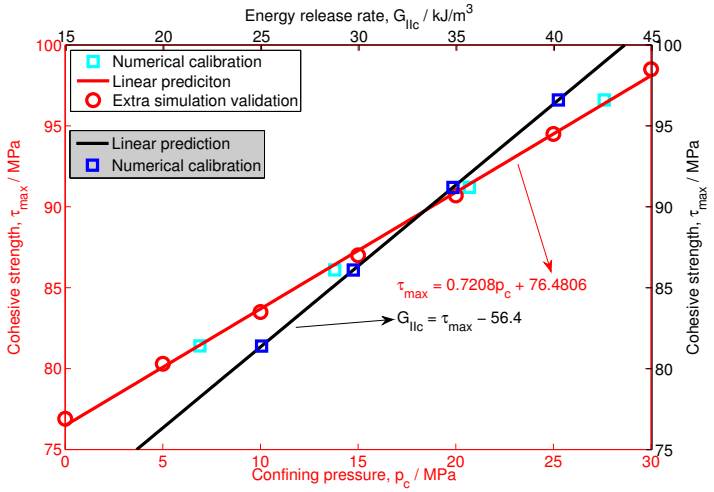

Figure 16. Linear interpolation curves relating CZM shear strength τ_{max}, shear energy release rate G_{IIc} and confining pressure p_c.

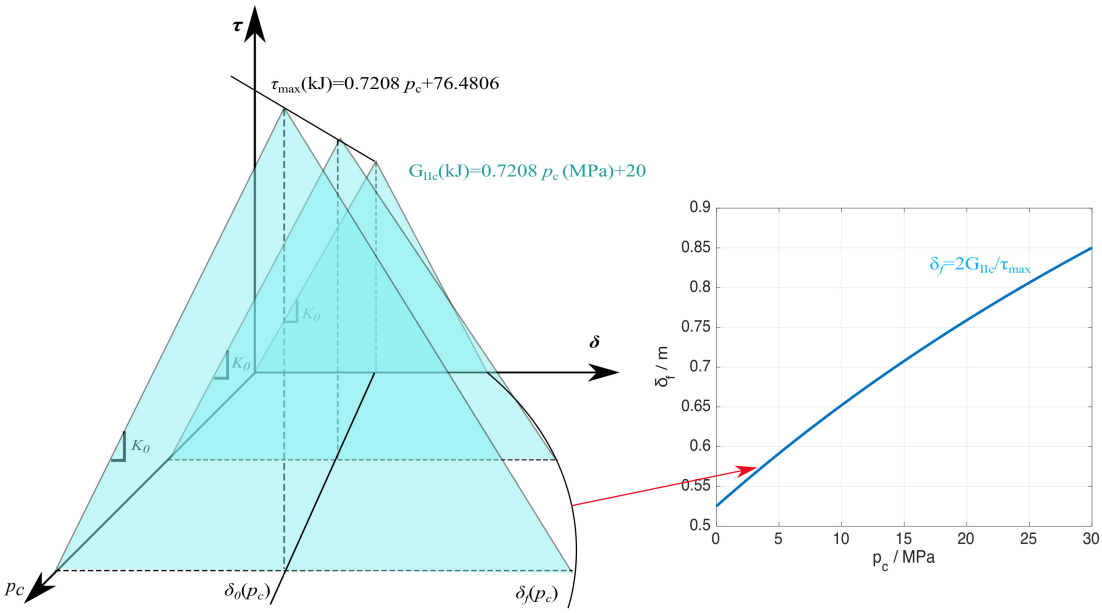

Figure 17. CZM failure envelope, modified from the bilinear cohesive zone model to account for confining pressure.

5. SIMULATION OF FRACTURE PROPAGATION IN MODE II WITH PROCESS ZONE

In the previous sections, we showed how the parameters for both the CDM and CZM zones can be calibrated by using laboratory rock mechanics experiments and three-dimensional simulations. In the following section, we apply the CDM/CZM model to an idealized 2D direct shear problem. We perform 2D simulations of mode II fracture propagation in shale at various depths (i.e., for various normal pressures applied at the faces of the cohesive fracture). The domain and boundary conditions considered are shown in Figure 18. This idealized configuration may reflect a range of geological scenarios: (1) lateral slip on bonded layers due to a horizontal driving force, (2) shear activation of a rough fault (oriented optimally or inoptimally, as shown, depending on the vector Ps), or (3) spalling of a weakly confined block subject to asymmetric loading. We embedded a horizontal cohesive zone of zero thickness in the middle of a 4m high, 6m wide continuum domain that contained 2,160 rectangular Finite Elements. The bounding elements were assigned the DSID model, with the constitutive parameters reported in Table II. A fracture was pre-assigned on a length of 0.5m in the cohesive zone. Pure mode II bilinear cohesive zone elements were assigned calibrated values of stiffness, shear cohesive strength and shear energy release rate, as explained in the previous section. We simulated a shear test for two confining pressures: $p_c = 5MPa$ and $p_c = 25MPa$. For the critical continuum damage value calibrated for Bakken shale, we can use Figure 16 to determine the CZM numerical parameters: the cohesive zone shear strength is $80.3MPa$ at $p_c = 5MPa$ and $94.5MPa$ at $p_c = 25MPa$, and the cohesive zone shear energy release rate is $23.9kJ/m^3$ at $p_c = 5MPa$ and $38.1kJ/m^3$ at $p_c = 25MPa$.

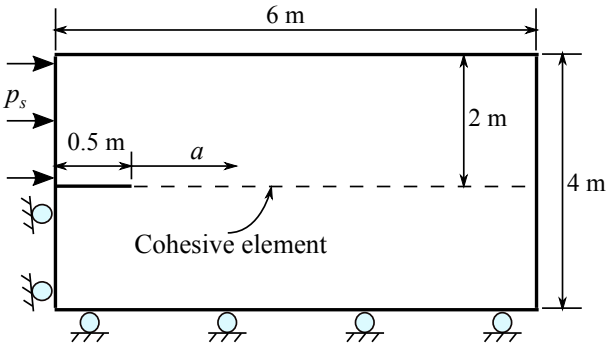

Figure 18. Geometry and boundary conditions adopted to simulate macro fracture propagation in mode II in shale.

Beyond the initial crack of 0.5 m, we note a the length of the completely debonded part of the cohesive zone, i.e. the position of the material crack tip (Figure 18). Figures 19 and 20 show the distributions of vertical micro-cracks (Ω_{11}) and horizontal micro-cracks (Ω_{22}) at several key stages of the propagation of the material crack tip. Due to the boundary conditions adopted in this simulation, the domain is subjected to horizontal compression in the top part and to horizontal tension in the bottom part, which results in the propagation of horizontal damage (Ω_{11}) below the cohesive zone. Vertical damage (Ω_{22}) concentrates around the cohesive zone, i.e. close to the shear plane. This is due to the damage criterion adopted in the DSID model: damage propagates when the differential stress exceeds the yield stress, which is reached at points of high stress concentration, close to the cohesive crack tip. The intensity of damage is higher for $p_c = 25\,MPa$ than for $p_c = 5\,MPa$. The observation of the propagation of the cohesive zone and of the damage zone for several values of a indicates that at low confining pressure ($p_c = 5\,MPa$), both the cohesive fracture and continuum damage propagate simultaneously, whereas at high confining pressure ($p_c = 25\,MPa$), the shear cohesive fracture propagates in a slip-friction mode, i.e. the dissipation process is a cycle of continuum damage propagation (which occurs when tensile differential stress exceeds the yield stress) and cohesive crack propagation (beyond the damaged zone). This difference of propagation mode explains why the distribution of damage is more uniform at low confining pressure.

Following the notations adopted in Equation 4, we define:

$$\begin{aligned} E_e &= \int_0^t \Big(\int_V \boldsymbol{\sigma} : \dot{\boldsymbol{\varepsilon}}^{el}\, \mathrm{d}V + \int_V \boldsymbol{\sigma} : \dot{\boldsymbol{\varepsilon}}^{ed}\, \mathrm{d}V \Big)\, \mathrm{d}\tau \\ E_{ir} &= \int_0^t \Big(\int_V \boldsymbol{\sigma} : \dot{\boldsymbol{\varepsilon}}^{id}\, \mathrm{d}V \Big)\, \mathrm{d}\tau \\ E_\Omega &= \int_0^t \Big(\int_V \boldsymbol{Y} : \dot{\boldsymbol{\Omega}}\, \mathrm{d}V \Big)\, \mathrm{d}\tau \\ E_c &= \int_0^t \Big(\int_S \boldsymbol{\sigma} : \boldsymbol{\delta}\, \mathrm{d}S \Big)\, \mathrm{d}\tau \end{aligned} \tag{32}$$

The total mechanical work input is equal to the sum of the elastic energy stored in the bounding

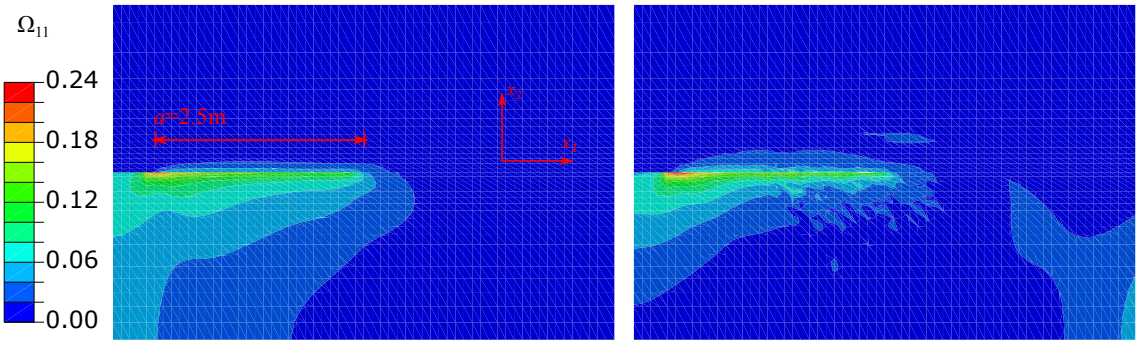

Figure 19. Horizontal damage (i.e. distribution of vertical micro-cracks, perpendicular to the x_1 axis) around the cohesive zone when the material crack tip reaches $a = 2.5m$, for $p_c = 5MPa$ (left) and $p_c = 25MPa$ (right).

material (E_e), the inelastic deformation energy dissipated in the bounding material (E_{ir}), the energy released by opening the micro-cracks (E_Ω) and the energy released by opening the cohesive fracture (E_c). For each finite element, we calculate E_e, E_{ir} and E_Ω by multiplying the mean value of the energy function considered by the area of the finite element. At the scale of the entire domain, E_e, E_{ir} and E_Ω are obtained by summing the energy of all the finite elements. We calculate E_c by multiplying the cohesive energy release rate by the cohesive crack length a. Note that we calculated the total energy cumulated and dissipated during the loading phase only, i.e. after applying the confining stress. As shown in Figure 21, the confining pressure affects the magnitude but not the evolution trend of the energy stored and dissipated. E_e, E_{ir}, E_Ω and E_c are about 1.4 larger under $p_c = 25\,MPa$ than under $p_c = 5\,MPa$ when the cohesive fracture tip reaches $a = 2.5\,m$. We verify that E_c is proportional to a, which is in agreement with the CZM shown in Figure 17. E_e mostly accumulates at the early stages of damage and cohesive crack propagation. E_{ir} is about three times smaller than E_e, and follows a trend similar to that of E_e. The energy dissipated by micro-crack debonding (E_Ω) is the only energy component that is smaller when $p_c = 25\,MPa$ than when $p_c = 5\,MPa$. We actually observe that under a confining pressure of 25 MPa, dissipation by micro-crack debonding nearly stops when a reaches 0.5 m. This observation is in agreement with the fracture propagation modes described above: at low confining pressure, continuum damage and cohesive crack propagate simultaneously, whereas at high confining pressure, the propagation of continuum damage alternates with that of cohesive crack (slip-friction mechanism).

Figure 22 compares the forms of energy dissipated during the propagation of the cohesive crack: $E_{in} = E_\Omega + E_{ir}$ is the total energy dissipated due to the propagation of continuum damage, and E_c is the energy dissipated by opening new material surfaces in the cohesive zone. It is worth being noted that the energy dissipated due to continuum damage propagation exceeds the energy dissipated by cohesive crack propagation. In the early stages of cohesive crack propagation, the evolution of the energy dissipated is the same for both confining pressures tested. In a second phase (when $E_c \simeq E_{in} > 6 \times 10^4\,J$), the energy dissipated by cohesive crack propagation is larger under high confining pressure than under low confining pressure for the same level of energy dissipated by continuum damage propagation.

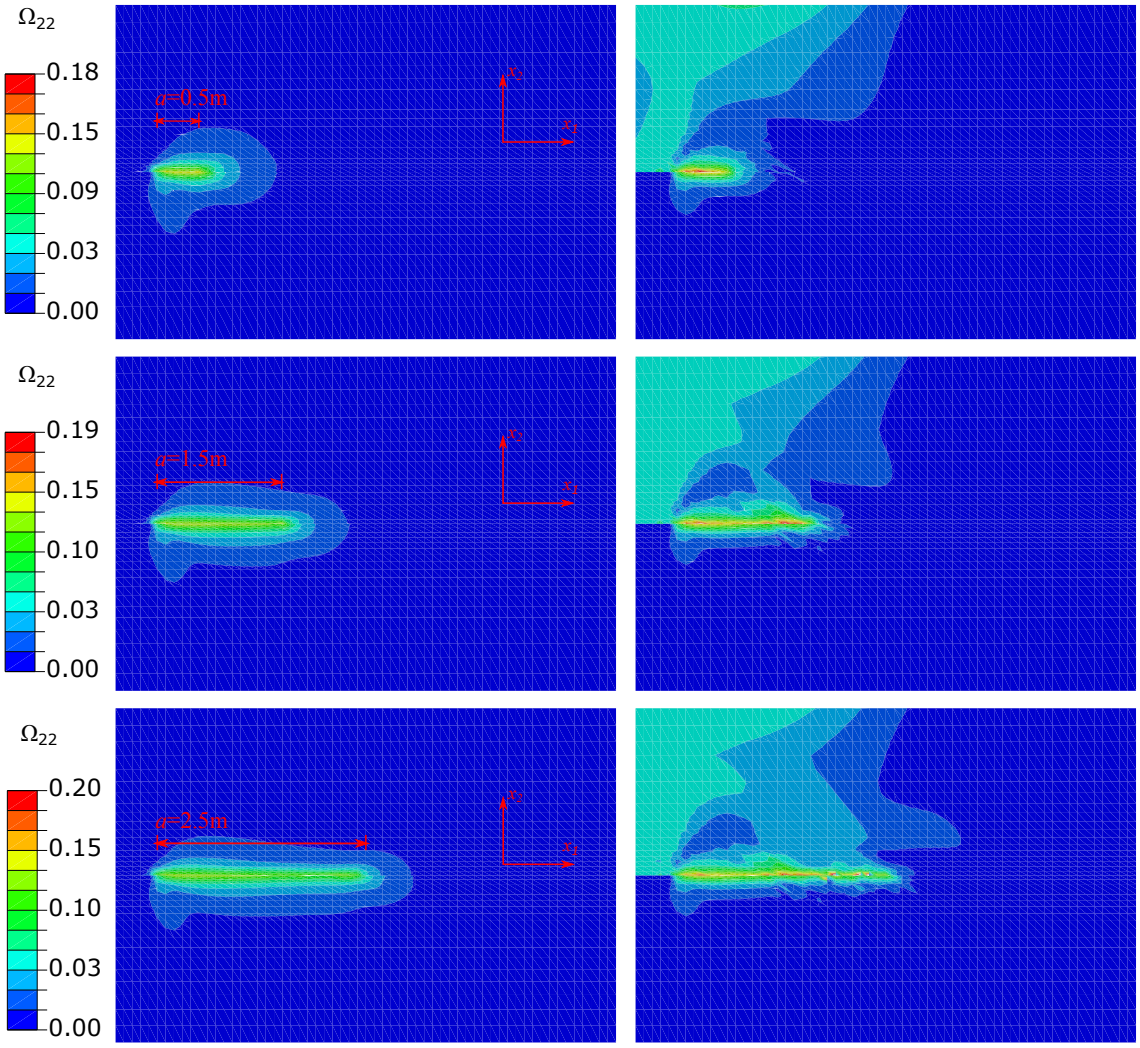

Figure 20. Vertical damage (i.e. distribution of horizontal micro-cracks, perpendicular to the x_2 axis) around the cohesive zone when the material crack tip reaches $a = 0.5m$, $a = 1.5m$ and $a = 2.5m$ for $p_c = 5MPa$ (left) and $p_c = 25MPa$ (right).

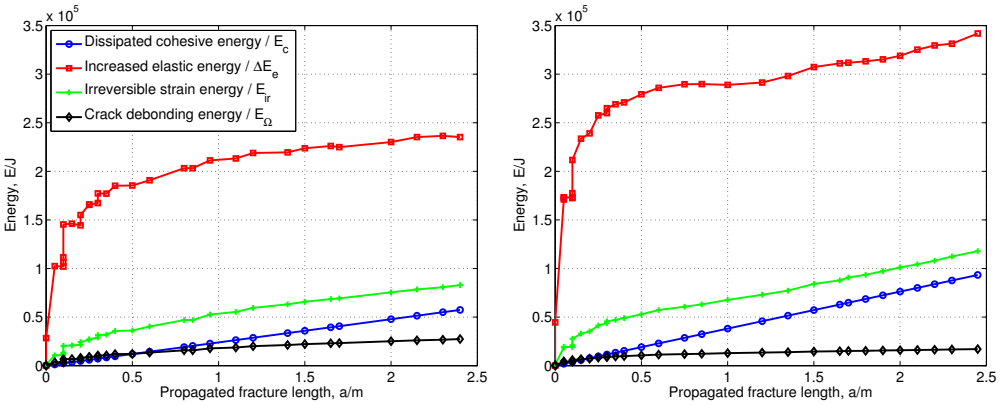

(a) Confining pressure $p_c = 5MPa$ (b) Confining pressure $p_c = 25MPa$

Figure 21. Evolution of the forms of energy stored and dissipated in the domain as the cohesive crack propagates.

This confirms again the propagation mechanisms noted earlier: simultaneous propagation of continuum damage and cohesive crack at low confining pressure or in the early stage of the shear loading performed at high confining pressure, and slip-friction mechanism in the later stage of the shear loading performed at high confining pressure.

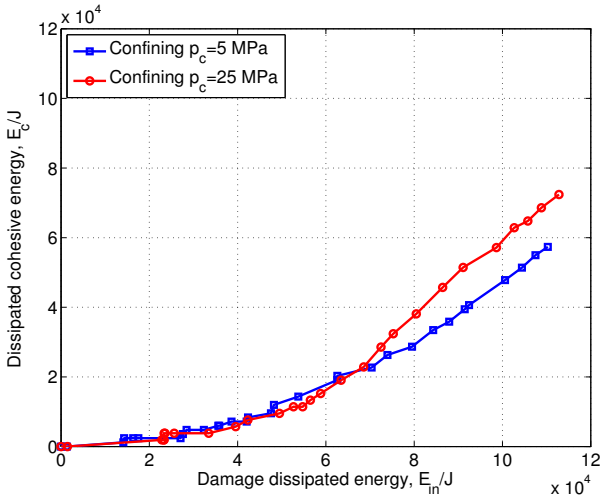

Figure 22. Comparison of the forms of energy dissipated during cohesive crack propagation in mode II: energy released by the creation of new material surfaces in the cohesive zone (E_c) and energy dissipated by continuum damage propagation (E_{in}).

6. CONCLUSION

In this paper, we proposed a strategy to simulate mode II fracture propagation at macro scale accompanied by micro crack evolution within the fracture process zone at meso scale for intact brittle material. A CZM is used to represent macro-fracture propagation. A CDM model, which represents micro-crack propagation, is calibrated against triaxial compression tests performed on Bakken shale, so as to reproduce the stress/strain curve before the failure peak. We simulate a direct shear test with the CDM model, which does not account for micro-crack interaction. We compare the damaged shear modulus with that obtained, in the same loading conditions, with Kachanov's micro-mechanical model, which accounts for micro-crack interaction. The results show that the critical damage threshold, at which crack interaction cannot be neglected, is equal to 0.3. The CZM is assigned a pure mode II bilinear cohesive law. The cohesive shear strength of the CZM is defined as the shear stress that marks the transition between smeared micro-crack propagation and crack coalescence followed by macro-crack propagation. We calibrate the cohesive shear strength by calculating the shear stress necessary to reach a CDM damage of 0.3 during direct shear tests performed on Bakken shale. We find that the shear cohesive strength of the CZM depends linearly on the confining pressure. Triaxial compression tests are simulated, in which the material sample is modeled as a FE CDM continuum that contains a CZM along the plane of weakness. The shear energy release rate of the CZM is fitted in order to match to the post-peak stress/strain curves obtained during experimental tests performed on Bakken shale. We find that the energy release rate depends linearly on the shear cohesive strength. Accordingly, we propose a modified failure envelope for the CZM to account for the dependence of the shear strength and energy release rate on confining pressure. The calibration procedure ensures that the coupled CZM/CDM model can capture the flow of energy that takes place between the bulk material that forms the matrix and the macroscopic fracture surfaces. We then show a simple application of the coupled damage propagation model by simulating the propagation of a meter-scale mode II fracture. Under low confining pressure, the macroscopic crack (CZM) and its damaged zone (CDM) propagate simultaneously (i.e. during the same loading increments). Under high confining pressure, we observe slip-friction fracture propagation, i. e. the debonding of the cohesive zone alternates with the propagation of continuum damage. Hence the proposed CZM/CDM model captures important tectonic features. Original contributions made in this paper include: (1) A thermodynamic analysis of the energy transfers between a fracture and a bounding continuum subject to softening and irreversible deformation; (2) A consistent calibration procedure for a model that accounts not only for the interaction between a fracture and its damage zone, but also for the transition from continuum damage to macro-scale fracture; (3) A Finite Element model of fracture propagation in a dynamic damage zone, which can distinguish continuous and stick-slip propagation modes. We are currently extending the formulation to the propagation of fractures in mode I and in mixed mode, in order to apply this computational method to the design of geological storage and hydraulic fracturing systems.

ACKNOWLEDGEMENTS

Funding to complete this research work was received from ConocoPhillips, Houston, TX.

REFERENCES

1. Chen Z. Finite element modelling of viscosity-dominated hydraulic fractures. Journal of Petroleum Science and Engineering 2012; **88**:136–144.
2. Haddad M, Sepehrnoori K. Simulation of hydraulic fracturing in quasi-brittle shale formations using characterized cohesive layer: Stimulation controlling factors. Journal of Unconventional Oil and Gas Resources 2015; **9**:65–83.
3. Jin W, Xu H, Arson C. Energy dissipation during mode i fracture propagation in shale: Comparison between a continuum damage model, a cohesive zone model and the extended finite element method. Shale Symposium at the International Congress of the ISRM Montreal, Canada, 2015.
4. Florez-Nino JM. Integrating geology, rock physics, and seismology for reservoir-quality prediction. PhD Thesis, Stanford University 2005.
5. Zehnder AT. Lecture notes on fracture mechanics. Citeseer, 2007.
6. Halm D, Dragon A. An anisotropic model of damage and frictional sliding for brittle materials. European Journal of Mechanics-A/Solids 1998; **17**(3):439–460.
7. Xu H, Arson C. Anisotropic damage models for geomaterials: theoretical and numerical challenges. International Journal of Computational Methods 2014; **11**(02):1342 007.
8. Kachanov M. Continuum model of medium with cracks. Journal of the Engineering Mechanics Division 1980; **106**(5):1039–1051.
9. Pensée V, Kondo D, Dormieux L. Micromechanical analysis of anisotropic damage in brittle materials. Journal of Engineering Mechanics 2002; **128**(8):889–897.
10. Halm D, Dragon A. A model of anisotropic damage by mesocrack growth; unilateral effect. International Journal of Damage Mechanics 1996; **5**(4):384–402.
11. Zhu C, Arson C. A model of damage and healing coupling halite thermo-mechanical behavior to microstructure evolution. Geotechnical and Geological Engineering 2014; :1–22.
12. Paliwal B, Ramesh K. An interacting micro-crack damage model for failure of brittle materials under compression. Journal of the Mechanics and Physics of Solids 2008; **56**(3):896–923.
13. Paredes JA, Barbat AH, Oller S. A compression–tension concrete damage model, applied to a wind turbine reinforced concrete tower. Engineering Structures 2011; **33**(12):3559–3569.
14. Arson C, Gatmiri B. Thermo-hydro-mechanical modeling of damage in unsaturated porous media: Theoretical framework and numerical study of the EDZ. International Journal for Numerical and Analytical Methods in Geomechanics 2012; **36**(3):272–306.
15. Comi C, Perego U. Fracture energy based bi-dissipative damage model for concrete. International Journal of Solids and Structures 2001; **38**(36):6427–6454.
16. Rice JR. A path independent integral and the approximate analysis of strain concentration by notches and cracks. Journal of Applied Mechanics 1968; **35**(2):379–386.
17. Hillerborg A, Modéer M, Petersson PE. Analysis of crack formation and crack growth in concrete by means of fracture mechanics and finite elements. Cement and Concrete Research 1976; **6**(6):773–781.
18. Gurtin ME. Thermodynamics and the cohesive zone in fracture. Zeitschrift für angewandte Mathematik und Physik ZAMP 1979; **30**(6):991–1003.
19. Barenblatt GI. The mathematical theory of equilibrium cracks in brittle fracture. Advances in Applied Mechanics 1962; **7**(1):55–129.
20. Xu XP, Needleman A. Numerical simulations of fast crack growth in brittle solids. Journal of the Mechanics and Physics of Solids 1994; **42**(9):1397–1434.
21. Tvergaard V, Hutchinson J. Effect of strain-dependent cohesive zone model on predictions of crack growth resistance. International Journal of Solids and Structures 1996; **33**(20):3297–3308.
22. Nielsen KL, Hutchinson JW. Cohesive traction–separation laws for tearing of ductile metal plates. International Journal of Impact Engineering 2012; **48**:15–23.
23. Woelke P, Shields M, Hutchinson J. Cohesive zone modeling and calibration for mode I tearing of large ductile plates. Engineering Fracture Mechanics 2015; .
24. Song SH, Paulino GH, Buttlar WG. A bilinear cohesive zone model tailored for fracture of asphalt concrete considering viscoelastic bulk material. Engineering Fracture Mechanics 2006; **73**(18):2829–2848.

25. Park K, Paulino GH. Cohesive zone models: a critical review of traction-separation relationships across fracture surfaces. Applied Mechanics Reviews 2011; **64**(6):060 802.
26. Park K, Paulino GH, Roesler JR. A unified potential-based cohesive model of mixed-mode fracture. Journal of the Mechanics and Physics of Solids 2009; **57**(6):891–908.
27. Park K, Paulino GH. Computational implementation of the PPR potential-based cohesive model in abaqus: educational perspective. Engineering Fracture Mechanics 2012; **93**:239–262.
28. Spring DW, Paulino GH. A growing library of three-dimensional cohesive elements for use in abaqus. Engineering Fracture Mechanics 2014; **126**:190–216.
29. Elices M, Guinea G, Gomez J, Planas J. The cohesive zone model: advantages, limitations and challenges. Engineering Fracture Mechanics 2002; **69**(2):137–163.
30. Qiao P, Chen Y. Cohesive fracture simulation and failure modes of FRP–concrete bonded interfaces. Theoretical and Applied Fracture Mechanics 2008; **49**(2):213–225.
31. Liu ZH, Shen W. Experimental study of fracture under combined modes K_I–K_{III}. International Journal of Fracture 1984; **25**(1):R21–R29.
32. Fakhimi A, Tarokh A. Process zone and size effect in fracture testing of rock. International Journal of Rock Mechanics and Mining Sciences 2013; **60**:95–102.
33. Valko P, Economides M, et al.. Applications of a continuum damage mechanics model to hydraulic fracturing. Low Permeability Reservoirs Symposium, Society of Petroleum Engineers, 1993.
34. Valkó P, Economides M. Propagation of hydraulically induced fractures—a continuum damage mechanics approach. International Journal of Rock Mechanics and Mining Sciences & Geomechanics Abstracts, vol. 31, Elsevier, 1994; 221–229.
35. Mazars J, Pijaudier-Cabot G. From damage to fracture mechanics and conversely: a combined approach. International Journal of Solids and Structures 1996; **33**(20):3327–3342.
36. Jirasek M, Zimmermann T. Embedded crack model: I. basic formulation. International Journal for Numerical Methods in Engineering 2001; **50**(6):1269–1290.
37. Jirasek M, Zimmermann T. Embedded crack model. Part II: Combination with smeared cracks. International Journal for Numerical Methods in Engineering 2001; **50**(6):1291–1305.
38. Comi C, Mariani S, Perego U. From localized damage to discrete cohesive crack propagation in nonlocal continua. Proceedings of the Fifth World Congress on Computational Mechanics (WCCM V), Vienna University of Technology, 2002.
39. Comi C, Mariani S, Perego U. An extended fe strategy for transition from continuum damage to mode I cohesive crack propagation. International Journal for Numerical and Analytical Methods in Geomechanics 2007; **31**(2):213.
40. Simone A, Wells GN, Sluys LJ. From continuous to discontinuous failure in a gradient-enhanced continuum damage model. Computer Methods in Applied Mechanics and Engineering 2003; **192**(41):4581–4607.
41. Cazes F, Coret M, Combescure A, Gravouil A. A thermodynamic method for the construction of a cohesive law from a nonlocal damage model. International Journal of Solids and Structures 2009; **46**(6):1476–1490.
42. Cuvilliez S, Feyel F, Lorentz E, Michel-Ponnelle S. A finite element approach coupling a continuous gradient damage model and a cohesive zone model within the framework of quasi-brittle failure. Computer Methods in Applied Mechanics and Engineering 2012; **237**:244–259.
43. Nguyen VP, Stroeven M, Sluys LJ. An enhanced continuous–discontinuous multiscale method for modeling mode-I cohesive failure in random heterogeneous quasi-brittle materials. Engineering Fracture Mechanics 2012; **79**:78–102.
44. Xu H, Arson C. Mechanistic analysis of rock damage anisotropy and rotation around circular cavities. Rock Mechanics and Rock Engineering 2015; :1–17.
45. Simo J, Ju J. Strain-and stress-based continuum damage models—I. formulation. International Journal of Solids and Structures 1987; **23**(7):821–840.
46. Shao J, Hoxha D, Bart M, Homand F, Duveau G, Souley M, Hoteit N. Modelling of induced anisotropic damage in granites. International Journal of Rock Mechanics and Mining Sciences 1999; **36**(8):1001–1012.
47. Dragon A, Halm D, Désoyer T. Anisotropic damage in quasi-brittle solids: modelling, computational issues and applications. Computer Methods in Applied Mechanics and Engineering 2000; **183**(3):331–352.
48. Chiarelli AS, Shao JF, Hoteit N. Modeling of elastoplastic damage behavior of a claystone. International Journal of Plasticity 2003; **19**(1):23–45.
49. Shao JF, Zhou H, Chau K. Coupling between anisotropic damage and permeability variation in brittle rocks. International Journal for Numerical and Analytical Methods in Geomechanics 2005; **29**(12):1231–1247.
50. Alfano G. On the influence of the shape of the interface law on the application of cohesive-zone models. Composites Science and Technology 2006; **66**(6):723–730.
51. Li H, Chandra N. Analysis of crack growth and crack-tip plasticity in ductile materials using cohesive zone models. International Journal of Plasticity 2003; **19**(6):849–882.
52. Volokh KY. Comparison between cohesive zone models. Communications in Numerical Methods in

Engineering 2004; **20**(11):845–856.
53. Shet C, Chandra N. Analysis of energy balance when using cohesive zone models to simulate fracture processes. Journal of Engineering Materials and Technology 2002; **124**(4):440–450.
54. Amendt D, Busetti S, Wenning Q, et al.. Mechanical characterization in unconventional reservoirs: A facies-based methodology. Petrophysics 2013; **54**(05):457–464.
55. Ortiz M, Simo J. An analysis of a new class of integration algorithms for elastoplastic constitutive relations. International Journal for Numerical Methods in Engineering 1986; **23**(3):353–366.
56. Simo J, Hughes TJ. Computational Inelasticity, chap. 7. Springer-Verlag, Berlin, 1998.
57. Turon A, Davila CG, Camanho PP, Costa J. An engineering solution for mesh size effects in the simulation of delamination using cohesive zone models. Engineering Fracture Mechanics 2007; **74**(10):1665–1682.
58. Kachanov M. Elastic solids with many cracks: a simple method of analysis. International Journal of Solids and Structures 1987; **23**(1):23–43.
59. Kachanov M. Effective elastic properties of cracked solids: critical review of some basic concepts. Applied Mechanics Reviews 1992; **45**(8):304–335.
60. Shen L, Yi S. New solutions for effective elastic moduli of microcracked solids. International Journal of Solids and Structures 2000; **37**(26):3525–3534.
61. Shen L, Li J. A numerical simulation for effective elastic moduli of plates with various distributions and sizes of cracks. International Journal of Solids and Structures 2004; **41**(26):7471–7492.
62. Borja RI, Foster CD. Continuum mathematical modeling of slip weakening in geological systems. Journal of Geophysical Research: Solid Earth 2007; **112**(B4).